Available online at www.sciencedirect.com

ScienceDirect

Geochimica et Cosmochimica Acta 201 (2017) 6–24

Geochimica et Cosmochimica Acta

www.elsevier.com/locate/gca

Calcium-aluminum-rich inclusions with fractionation and unidentified nuclear effects (FUN CAIs): II. Heterogeneities of magnesium isotopes and ^{26}Al in the early Solar System inferred from *in situ* high-precision magnesium-isotope measurements

Changkun Park [a,b,*], Kazuhide Nagashima [a], Alexander N. Krot [a], Gary R. Huss [a], Andrew M. Davis [c], Martin Bizzarro [d]

[a] *Hawai'i Institute of Geophysics and Planetology, School of Ocean, Earth Science and Technology, University of Hawai'i at Mānoa, Honolulu, HI 96822, USA*

[b] *Division of Earth-System Sciences, Korea Polar Research Institute, Incheon 21990, Republic of Korea*

[c] *Department of the Geophysical Sciences, Enrico Fermi Institute, and Chicago Center for Cosmochemistry, University of Chicago, 5734 South Ellis Avenue, Chicago, IL 60637-1433, USA*

[d] *Centre for Star and Planet Formation, Geological Museum, University of Copenhagen, Øster Voldgade 5-7, DK-1350, Denmark*

Received 1 March 2016; accepted in revised form 1 October 2016; available online 8 October 2016

Abstract

Calcium-aluminum-rich inclusions with isotopic mass fractionation effects and unidentified nuclear isotopic anomalies (FUN CAIs) have been studied for more than 40 years, but their origins remain enigmatic. Here we report *in situ* high precision measurements of aluminum-magnesium isotope systematics of FUN CAIs by secondary ion mass spectrometry (SIMS). Individual minerals were analyzed in six FUN CAIs from the oxidized CV3 carbonaceous chondrites Axtell (compact Type A CAI *Axtell 2271*) and Allende (Type B CAIs *C1* and *EK1-4-1*, and forsterite-bearing Type B CAIs *BG82DH8*, *CG-14*, and *TE*). Most of these CAIs show evidence for excess ^{26}Mg due to the decay of ^{26}Al. The inferred initial ^{26}Al/^{27}Al ratios [$(^{26}Al/^{27}Al)_0$] and the initial magnesium isotopic compositions ($\delta^{26}Mg_0$) calculated using an exponential law with an exponent β of 0.5128 are $(3.1 \pm 1.6) \times 10^{-6}$ and 0.60 ± 0.10‰ (*Axtell 2271*), $(3.7 \pm 1.5) \times 10^{-6}$ and -0.20 ± 0.05‰ (*BG82DH8*), $(2.2 \pm 1.1) \times 10^{-6}$ and -0.18 ± 0.05‰ (*C1*), $(2.3 \pm 2.4) \times 10^{-5}$ and -2.23 ± 0.37‰ (*EK1-4-1*), $(1.5 \pm 1.1) \times 10^{-5}$ and -0.42 ± 0.08‰ (*CG-14*), and $(5.3 \pm 0.9) \times 10^{-5}$ and -0.05 ± 0.08‰ (*TE*) with 2σ uncertainties. We infer that FUN CAIs recorded heterogeneities of magnesium isotopes and ^{26}Al in the CAI-forming region(s). Comparison of ^{26}Al-^{26}Mg systematics, stable isotope (oxygen, magnesium, calcium, and titanium) and trace element studies of FUN and non-FUN igneous CAIs indicates that there is a continuum among these CAI types. Based on these observations and evaporation experiments on CAI-like melts, we propose a generic scenario for the origin of igneous (FUN and non-FUN) CAIs: (*i*) condensation of isotopically normal solids in an ^{16}O-rich gas of approximately solar composition; (*ii*) formation of CAI precursors by aggregation of these solids together with variable abundances of isotopically anomalous grains—possible carriers of unidentified nuclear (UN)

* Corresponding author at: Division of Earth-System Sciences, Korea Polar Research Institute, Incheon 21990, Republic of Korea. *E-mail address:* changkun@kopri.re.kr (C. Park).

http://dx.doi.org/10.1016/j.gca.2016.10.002

effects; and (*iii*) melt evaporation of these precursors accompanied by crystallization under different temperatures and gas pressures, leading to the observed variations in mass-dependent isotopic fractionation (F) effects.

Keywords: Fractionation and unidentified nuclear effects (FUN); CAI; ^{26}Al; Magnesium isotopes; Heterogeneities of magnesium-isotopes and ^{26}Al; Early Solar System

1. INTRODUCTION

Calcium-aluminum-rich inclusions (CAIs) with crystallization ages of ~4567 Ma from the CV (Vigarano-like) carbonaceous chondrites are the oldest Solar System solids dated (e.g., Connelly et al., 2012). Since the discovery of excess ^{26}Mg due to the *in situ* decay of a short-lived radionuclide ^{26}Al (half-life ~0.7 Ma) in a CAI from the oxidized Allende CV3 chondrite (Lee et al., 1977), most CV CAIs have been shown to contain excess ^{26}Mg with an abundance corresponding to an initial ^{26}Al/^{27}Al ratio, $(^{26}Al/^{27}Al)_0$, of $\sim 5 \times 10^{-5}$, called the "canonical" ratio (MacPherson et al., 1995). Recent magnesium-isotope studies of bulk CAIs from Allende by multicollector inductively coupled plasma mass spectrometry (MC ICP-MS) revealed that on an ^{26}Al-^{26}Mg evolutionary diagram, CV CAIs plot along a regression line (model isochron) with a slope corresponding to an $(^{26}Al/^{27}Al)_0$ ratio of $(5.23 \pm 0.13) \times 10^{-5}$ and an intercept corresponding to an initial magnesium isotopic composition ($\delta^{26}Mg_0$) of -0.040 ± 0.029‰ (Jacobsen et al., 2008a). High-precision secondary ion mass spectrometry (SIMS) analyses of magnesium isotopes in two unmelted CAIs from Vigarano yielded internal isochrons with $(^{26}Al/^{27}Al)_0$ of $(5.13 \pm 0.11) \times 10^{-5}$ and $(5.29 \pm 0.28) \times 10^{-5}$, and $\delta^{26}Mg_0$ of -0.020 ± 0.015‰ and -0.07 ± 0.11‰, respectively (MacPherson et al., 2012). These observations are often interpreted as evidence for a uniform distribution of ^{26}Al (at the canonical level) and magnesium isotopes ($\delta^{26}Mg_0 \sim -0.04$‰) in the protoplanetary disk (e.g., Jacobsen et al., 2008a; MacPherson et al., 2012; Mishra and Chaussidon, 2014). Based on the high-precision magnesium isotope measurements of bulk CAIs and AOAs from the reduced CV3 chondrite Efremovka using MC ICP-MS, Larsen et al. (2011) reported $(^{26}Al/^{27}Al)_0$ of $(5.25 \pm 0.02) \times 10^{-5}$ and $\delta^{26}Mg_0$ of -0.0159 ± 0.0014‰. This $\delta^{26}Mg_0$ is quite different from the value of -0.038‰ predicted from a uniform distribution of ^{26}Al with $(^{26}Al/^{27}Al)_0$ of 5.23×10^{-5} and a solar ^{27}Al/^{24}Mg ratio of 0.101 (Larsen et al., 2011). Based on these observations and variable amounts of radiogenic ^{26}Mg ($\delta^{26}Mg^*$) of bulk chondrites having approximately solar ^{27}Al/^{24}Mg ratios, these authors concluded that magnesium isotopes were heterogeneously distributed in the protoplanetary disk and attributed this heterogeneity solely to a heterogeneous distribution of ^{26}Al.

Large mass-dependent isotopic fractionations and isotopic anomalies in magnesium and oxygen have been discovered in two Allende CAIs, *C1* and *EK1-4-1*, which were designated as FUN (fractionation and unidentified nuclear effects) inclusions (Lee et al., 1976; Clayton and Mayeda, 1977; Wasserburg et al., 1977). Later, refractory inclusions with large mass-dependent fractionation effects in magnesium, silicon, and oxygen isotopes, and non-mass-dependent isotopic anomalies in magnesium, calcium, titanium, chromium, strontium, barium, neodymium, and samarium, have been regarded as FUN CAIs (McCulloch and Wasserburg, 1978a,b; Papanastassiou and Wasserburg, 1978; Lee et al., 1979, 1980; Niederer et al., 1981, 1985; Clayton et al., 1984; Niederer and Papanastassiou, 1984; Papanastassiou, 1986; Ireland and Compston, 1987; Papanastassiou and Brigham, 1987; Brigham, 1990; Davis et al., 1991; Ireland et al., 1992; Loss et al., 1994; Srinivasan et al., 2000; Ushikubo et al., 2007; Hiyagon and Hashimoto, 2008; Thrane et al., 2008; Liu et al., 2009; Makide et al., 2009; Krot et al., 2010, 2014; Marin-Carbonne et al., 2012; Williams et al., 2012, 2013; Fukuda et al., 2013; Holst et al., 2013). FUN CAIs are typically characterized by low $(^{26}Al/^{27}Al)_0$ ($<<\sim 5 \times 10^{-5}$) and deficits in $\delta^{26}Mg_0$ (Wasserburg et al., 1977; Esat et al., 1978; see MacPherson et al., 1995) relative the inferred initial Solar System value(s) (Jacobsen et al., 2008a; Larsen et al., 2011). The low $(^{26}Al/^{27}Al)_0$ in FUN CAIs has been attributed either to their late formation, after nearly complete decay of ^{26}Al (e.g., Lee et al., 1979), or to their early formation prior to and during addition of ^{26}Al to the protoplanetary disk (Fahey et al., 1987; Sahijpal and Goswami, 1998; Thrane et al., 2008; Holst et al., 2013). The deficits in $\delta^{26}Mg_0$ in FUN CAIs are interpreted as due to incomplete mixing of isotopically anomalous grains from different stellar sources (Wasserburg et al., 1977). Therefore, studies of the aluminum-magnesium isotopic systematics of FUN CAIs are of great importance for understanding the distributions of ^{26}Al and magnesium isotopes in the CAI-forming region(s) of the protoplanetary disk and may also provide constraints on the isotopic compositions of the CAI forming region(s) and the time–temperature histories leading to mass-dependent fractionation.

Most of the early magnesium-isotope studies of FUN CAIs were performed by thermal ionization mass spectrometry (TIMS) (e.g., Wasserburg et al., 1977; Esat et al., 1978; Lee et al., 1979; Brigham, 1990), and small geometry SIMS instruments (e.g., Hutcheon, 1982; Fahey et al., 1987; Srinivasan et al., 2000). Recent advances in SIMS with large geometry and multicollector (MC) systems allow *in situ* high-precision and high accuracy measurements of magnesium isotopes in individual minerals of refractory inclusions (e.g., Makide et al., 2009; Kita et al., 2012; MacPherson et al., 2012; Mishra and Chaussidon, 2014). To understand the origin of FUN CAIs, we performed combined mineralogical, petrographic, isotopic (aluminum-magnesium, oxygen, calcium, titanium, and silicon), and trace element studies of twelve CAIs previously identified as FUN inclusions. Here we report on the *in situ* aluminum-magnesium isotope measurements of

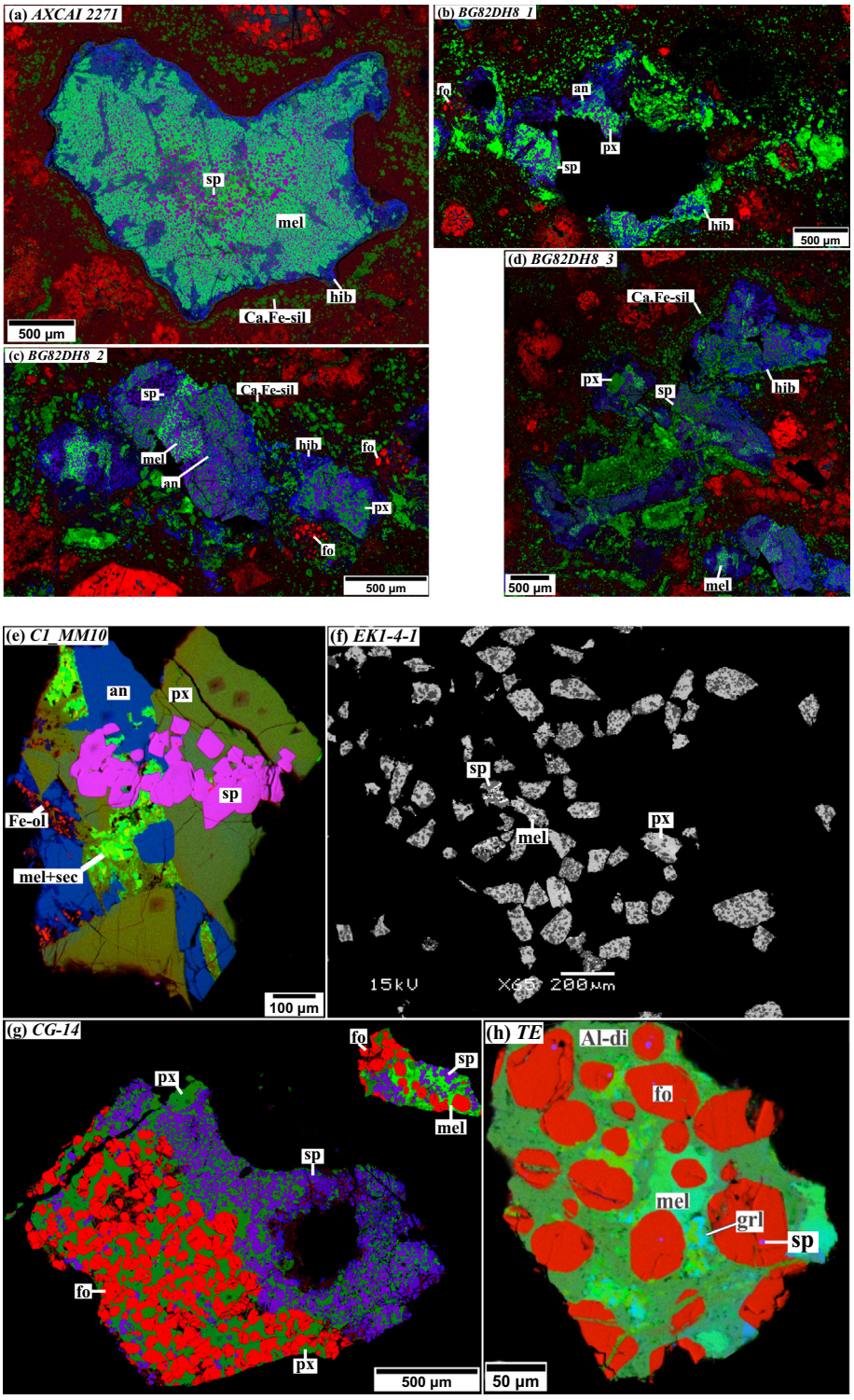

Fig. 1. Combined elemental maps in Mg (red), Ca (green), and Al (blue) Kα x-rays (a–e, g, h) and backscattered electron image (f) of the FUN CAIs *AXCAI 2271* (a), *BG82DH8* (b–d), *C1* (e), *EK1-4-1* (f), *CG-14* (g), and *TE* (h). Al-di = titanium-free, aluminum-rich diopside; an = anorthite; Ca,Fe-sil = secondary calcium-, iron-rich silicates; Fe-ol = ferroan olivine; fo = calcium-rich forsterite; grl = grossular; hib = hibonite; mel = melilite; px = fassaite; sec = unidentified secondary phases; sp = spinel. (For interpretation of the references to color in this figure legend, the reader is referred to the web version of this article.)

individual minerals in six previously identified FUN CAIs from the oxidized CV3 chondrites Allende and Axtell (Wasserburg et al., 1977; Esat et al., 1978; Clayton et al., 1984; Papanastassiou and Brigham, 1989; Brigham, 1990; Srinivasan et al., 2000) made with the University of Hawai'i (UH) Cameca ims-1280.

2. ANALYTICAL TECHNIQUES

2.1. Samples

The six FUN CAIs measured for aluminum-magnesium isotopic compositions include *Axtell 2271* from Axtell, and *BG82DH8*, *C1*, *EK1-4-1*, *CG-14*, and *TE* from Allende (Fig. 1). The "sections" of *C1*, *EK1-4-1*, *CG-14*, and *TE* consist of fragments left after previous isotope studies with TIMS and gas-source mass spectrometry. The mineralogy, petrography, and oxygen isotopic compositions of these CAIs have been recently reported by Krot et al. (2014) and we only briefly summarize their mineralogy and petrography.

2.2. Aluminum-magnesium isotope measurements

Aluminum- and magnesium-isotope compositions were measured *in situ* with the UH Cameca ims-1280 SIMS. Primary $^{16}O^-$ ions sputtered the sample surface with an impact energy of 23 keV. Positive secondary ions were accelerated to 10 keV. An energy window of 55 eV was used. Two analytical procedures were used to measure aluminum-magnesium isotopic systematics in minerals with low and high $^{27}Al/^{24}Mg$ ratios.

Minerals with low $^{27}Al/^{24}Mg$ ratios (aluminum-, titanium-diopside (hereafter fassaite), åkermanitic melilite, forsterite, and spinel) were analyzed with an $^{16}O^-$ primary beam of ~20–30 μm diameter. The primary current was set to ~5 nA for forsterite and spinel, ~8 nA for fassaite, and ~15 nA for åkermanitic melilite. The mass resolving power (MRP) was set to ~2400 with exit slit of 500 μm, sufficient to separate interferences of $^{48}Ca^{++}$ and $^{23}NaH^+$ from $^{24}Mg^+$. Although this setting does not allow a complete separation of $^{25}Mg^+$ from $^{24}MgH^+$ interference, a contribution of $^{24}MgH^+$ onto $^{25}Mg^+$ was estimated to be less than 1 ppm. Four multicollection Faraday cups (FCs) were used to detect $^{24}Mg^+$, $^{25}Mg^+$, $^{26}Mg^+$, and $^{27}Al^+$, simultaneously, with the magnetic field controlled by a nuclear magnetic resonance (NMR) probe. Each analysis consisted of 30 cycles with a counting time of 10 s per cycle. Automated centering of the secondary beam in the 5000-μm-diameter field aperture and high-voltage offset control were applied before each measurement.

Minerals with high $^{27}Al/^{24}Mg$ ratios (anorthite and hibonite) were analyzed with an $^{16}O^-$ primary beam focused to ~5–8 μm diameter with a current of ~40 pA for hibonite and ~200 pA for anorthite. Secondary $^{24}Mg^+$, $^{25}Mg^+$, and $^{26}Mg^+$ ions were measured with a monocollection electron multiplier in peak jumping mode, and $^{27}Al^+$ ions were measured with a multicollection FC, simultaneously with $^{25}Mg^+$ measurement. Counting times were 4 s for $^{24}Mg^+$ and 10 s for others, and the measurements consisted of 120 cycles. Entrance and exit slits were set to obtain the MRP of ~3700, sufficient to separate interferences of $^{48}Ca^{++}$ and hydrides ($^{23}NaH^+$ and $^{24}MgH^+$) from magnesium-isotope signals. Automated beam centering in the field aperture, mass-peak centering, and high-voltage offset control were applied after presputtering of 300–480 s. The mass-peak centering and offset control were also applied at cycle 40 and 80.

To measure the exact spots in small grains of hibonite and avoid beam overlap with spinel intergrown with hibonite in the periphery of several FUN CAIs, we used the UH JEOL JSM-5900LV scanning electron microscope to mark the spots of interest in hibonite grains. The marking was done by burning the carbon coat on the hibonite grains with a focused electron beam operated at 20 kV for 5–10 min. This made a submicron-sized hole in the carbon-coat, which could be easily recognized as a hot spot in the $^{27}Al^+$ scanning ion images, obtained by rastering over 200 × 200 to 50 × 50 μm^2. The carbon coat is not removed during the scanning ion imaging because of the low sputter rate. The recognized spot of interest was subsequently centered to the exact position of the primary ion beam.

A deadtime correction of 30 ns was applied to data collected with the monocollection electron multiplier and background noise for FCs was corrected. Time-interpolation was applied to anorthite and hibonite measurements with a monocollection electron multiplier in peak jumping mode. Isotope ratios were calculated from total counts summed over the entire analysis to minimize the positive bias associated with low count rate in individual cycles (Ogliore et al., 2011).

In order to obtain an excess ^{26}Mg due to ^{26}Al decay and to resolve isotopic anomalies, we applied instrumental and intrinsic (natural) fractionation corrections, similar to those detailed in Makide et al. (2009). Instrumental mass fractionation (IMF) effects were corrected by standard-sample bracketing using San Carlos olivine, synthetic aluminum-titanium-pyroxene, synthetic melilite glass ($Åk_{\sim 30}$), Burma spinel, Miyake-jima anorthite, and Madagascar hibonite standards, assuming that all standards have terrestrial $^{25}Mg/^{24}Mg$ and $^{26}Mg/^{24}Mg$ ratios, 0.126896 and 0.139652, respectively (Bizzarro et al., 2011):

$$\left(\frac{^{i}Mg}{^{24}Mg}\right)^{sample}_{IMF-corr} = \left(\frac{^{i}Mg}{^{24}Mg}\right)^{sample}_{measured} \times \left[\frac{\left(\frac{^{i}Mg}{^{24}Mg}\right)_{terrestrial}}{\left(\frac{^{i}Mg}{^{24}Mg}\right)^{standard}_{measured}}\right], \quad (1)$$

where i = 25 and 26.

After IMF correction, magnesium isotopic compositions are reported as permil deviations from the terrestrial $^{25}Mg/^{24}Mg$ and $^{26}Mg/^{24}Mg$ ratios:

$$\delta^{i}Mg^{sample}_{IMF-corr} = \left[\frac{\left(\frac{^{i}Mg}{^{24}Mg}\right)^{sample}_{IMF-corr}}{\left(\frac{^{i}Mg}{^{24}Mg}\right)_{terrestrial}} - 1\right] \times 1000$$

$$= \left[\frac{\left(\frac{^{i}Mg}{^{24}Mg}\right)^{sample}_{measured}}{\left(\frac{^{i}Mg}{^{24}Mg}\right)^{standard}_{measured}} - 1\right] \times 1000. \quad (2)$$

FUN CAIs are expected to have intrinsic mass fractionation due to evaporation during melting and crystallization. The IMF-corrected $\delta^{25}Mg$ is assigned to the intrinsic mass fractionation of samples, F_{Mg} (‰/amu):

$$F_{Mg} = \delta^{25}Mg^{sample}_{IMF-corr} \cong \delta^{25}Mg^{sample}_{measured} - \delta^{25}Mg^{standard}_{measured} \quad (3)$$

where

$$\delta^{25}Mg^{\text{sample or standard}}_{\text{measured}} = \left[\frac{\left(\frac{^{i}Mg}{^{24}Mg}\right)^{\text{sample or standard}}_{\text{measured}}}{\left(\frac{^{i}Mg}{^{24}Mg}\right)_{\text{terrestrial}}} - 1\right] \times 1000$$

To determine the contribution of radiogenic ^{26}Mg to the measured $^{26}Mg/^{24}Mg$ ratio, the intrinsic mass fractionation was propagated from $^{25}Mg/^{24}Mg$ to $^{26}Mg/^{24}Mg$ using an exponential law with an exponent (β). First, the IMF-corrected ratios were converted to δ′-coordinates:

$$\delta^{i}Mg'^{\text{sample}}_{\text{IMF-corr}} = 1000 \times \ln\left[\frac{\left(\frac{^{i}Mg}{^{24}Mg}\right)^{\text{sample}}_{\text{IMF-corr}}}{\left(\frac{^{i}Mg}{^{24}Mg}\right)_{\text{terrestrial}}}\right] = 1000 \times \ln\left[\frac{\left(\frac{^{i}Mg}{^{24}Mg}\right)^{\text{sample}}_{\text{measured}}}{\left(\frac{^{i}Mg}{^{24}Mg}\right)^{\text{standard}}_{\text{measured}}}\right] \quad (4)$$

The fractionation-corrected $\delta^{26}Mg'^{*}$ was calculated from $\delta^{i}Mg'$, as a distance between $\delta^{25}Mg'^{\text{sample}}_{\text{IMF-corr}}$ and the point on a mass fractionation curve derived from $\delta^{25}Mg'^{\text{sample}}_{\text{IMF-corr}}$:

$$\delta^{26}Mg^{*\prime} = \delta^{26}Mg'^{\text{sample}}_{\text{IMF-corr}} - \left(\frac{1}{\beta}\right) \times \delta^{25}Mg'^{\text{sample}}_{\text{IMF-corr}} \quad (5)$$

$\delta^{26}Mg'^{*}$ was then converted to the fractionation-corrected $^{26}Mg/^{24}Mg$ ratio:

$$\left(\frac{^{26}Mg}{^{24}Mg}\right)^{\text{sample}}_{\text{FRAC-corr}} = \left(\frac{^{26}Mg}{^{24}Mg}\right)_{\text{terrestrial}} \times \exp(\delta^{26}Mg^{*\prime}/1000). \quad (6)$$

Lastly, the intrinsic-fractionation-corrected $^{26}Mg/^{24}Mg$ ratio was then converted into standard δ-notation, $\delta^{26}Mg^{*}$:

$$\delta^{26}Mg^{*} = \left[\frac{\left(\frac{^{26}Mg}{^{24}Mg}\right)^{\text{sample}}_{\text{FRAC-corr}}}{\left(\frac{^{26}Mg}{^{24}Mg}\right)_{\text{terrestrial}}} - 1\right] \times 1000. \quad (7)$$

Using Eqs. (4)–(6), $\left(^{26}Mg/^{24}Mg\right)^{\text{sample}}_{\text{FRAC-corr}}$ can be translated to,

$$\left(\frac{^{26}Mg}{^{24}Mg}\right)^{\text{sample}}_{\text{FRAC-corr}} = \left(\frac{^{26}Mg}{^{24}Mg}\right)_{\text{terrestrial}} \times \frac{\left(\frac{^{26}Mg}{^{24}Mg}\right)^{\text{sample}}_{\text{measured}}\Big/\left(\frac{^{26}Mg}{^{24}Mg}\right)^{\text{standard}}_{\text{measured}}}{\left[\left(\frac{^{25}Mg}{^{24}Mg}\right)^{\text{sample}}_{\text{measured}}\Big/\left(\frac{^{25}Mg}{^{24}Mg}\right)^{\text{standard}}_{\text{measured}}\right]^{1/\beta}} \quad (8)$$

From (7) and (8), $\delta^{26}Mg^{*}$ can be rewritten as

$$\delta^{26}Mg^{*} = \left[\frac{\left(\frac{^{26}Mg}{^{24}Mg}\right)^{\text{sample}}_{\text{measured}}\Big/\left(\frac{^{26}Mg}{^{24}Mg}\right)^{\text{standard}}_{\text{measured}}}{\left[\left(\frac{^{25}Mg}{^{24}Mg}\right)^{\text{sample}}_{\text{measured}}\Big/\left(\frac{^{25}Mg}{^{24}Mg}\right)^{\text{standard}}_{\text{measured}}\right]^{1/\beta}} - 1\right] \times 1000 = \left[\frac{1 + \delta^{26}Mg^{\text{sample}}_{\text{IMF-corr}}/1000}{\left(1 + \delta^{25}Mg^{\text{sample}}_{\text{IMF-corr}}/1000\right)^{1/\beta}} - 1\right] \times 1000 \quad (9)$$

Although we assume that all standards have terrestrial $^{25}Mg/^{24}Mg$ and $^{26}Mg/^{24}Mg$ ratios, these values do not play a role in Eq. (9) because they are all canceled out. We note that Eq. (9) is equivalent to the equation to calculate $\varepsilon^{26}Mg$ used in S. Jacobsen et al. (2008b).

The choice of the exponent β in the exponential law can make a significant difference in $\delta^{26}Mg^{*}$ values of minerals with low $^{27}Al/^{24}Mg$ ratios when their intrinsic mass fractionations are large. We used β of 0.5128 inferred from vacuum evaporation experiments of CAI-like melts (Davis et al., 2015) that is expected to best describe the highly fractionated magnesium-isotope composition of FUN CAIs. To explore the potential uncertainty on the $\delta^{26}Mg_0$ and $(^{26}Al/^{27}Al)_0$ values caused by the choice of β, we compare the results of calculations using 0.5128 with those using 0.511 and 0.514 (see Section 4.1.1).

The reported errors (2σ) include both the internal precision of an individual analysis (2SE; two standard error of the mean of measurement cycles) and the external reproducibility for standard measurements (2SD; two standard deviation) during a given analytical session. The $^{27}Al^{+}/^{24}Mg^{+}$ ratios measured with the ion microprobe were corrected using a relative sensitivity factor (RSF):

$$RSF = (^{27}Al^{+}/^{24}Mg^{+})_{\text{SIMS}}/(^{27}Al/^{24}Mg)_{\text{true}}. \quad (10)$$

The true $^{27}Al/^{24}Mg$ ratios of the terrestrial standards were determined from the Al/Mg ratios measured by electron microprobe.

3. RESULTS

Magnesium isotopic compositions of individual minerals in the FUN CAIs are listed in Table 1. The internal aluminum-magnesium isochrons are illustrated in Figs. 2–7. Images of all SIMS spots in minerals measured for aluminum-magnesium isotopic systematics are given in the Supplement Figures (Figs. S1–S6).

3.1. Axtell 2271

Three thin sections (labeled as *AXCAI 2271*, *2571*, and *2771*) from a compact Type A (CTA) FUN CAI *Axtell 2271* were originally described by Srinivasan et al. (2000). We studied sections *AXCAI 2271* and *2571*. The CAI consists mainly of melilite ($Åk_{9-36}$) poikilitically enclosing spinel and perovskite grains (Figs. 1a, S1a–h). The åkermanite content in melilite decreases from the CAI core towards the periphery. Spinel grains are preferentially concentrated in the central portion of the inclusion. The outermost part of the CAI consists of closely intergrown hibonite (4.9 wt% TiO_2, 3.0 wt% MgO) and spinel (Figs. S1i–l). Melilite in the outer portion of the CAI is partly replaced by nepheline, sodalite, grossular, and an unidentified needle-shaped secondary mineral, possibly dmisteinbergite (Park et al., 2013; Fintor et al., 2014).

Magnesium isotopes were measured in spinel, melilite, and hibonite in *AXCAI 2271* and only in hibonite in *AXCAI 2571*. Magnesium in spinel and melilite is highly fractionated (F_{Mg} ~14–17‰/amu), in good agreement with previously reported data (Srinivasan et al., 2000).

Table 1
Magnesium-isotope compositions of individual minerals and the inferred initial $^{26}Al/^{27}Al$ ratios, $(^{26}Al/^{27}Al)_0$, and initial magnesium-isotope compositions ($\delta^{26}Mg_0$) in FUN CAIs studied.

	This study								Previously reported data				
Inclusion	Mineral	Spot#	$^{27}Al/^{24}Mg$	$2\sigma_m$[a]	$\delta^{26}Mg^*$	$2\sigma_m$	F_{Mg}[b]	$2\sigma_m$		$\delta^{26}Mg^*$	2σ[c]	F_{Mg}	2σ
Axtell 2271	Spinel	#1	2.43	±0.03	0.53	±0.18	13.85	±0.16	Srinivasan et al. (2000)				
	Spinel	#2	2.41	±0.03	0.64	±0.15	14.69	±0.16	Spinel	−0.2	±1.9	14.3	±3.2
	Spinel	#3	2.45	±0.03	0.59	±0.18	16.69	±0.16	($n = 9$)				
	Melilite	#1	21.38	±0.40	1.02	±0.29	14.67	±0.16					
	Melilite	#2	7.90	±0.09	0.90	±0.20	15.17	±0.13					
	Melilite	#3	17.47	±0.18	0.94	±0.27	14.97	±0.15	Melilite	0.4	±3.0	14.2	±4.0
	Melilite	#4	8.52	±0.10	0.83	±0.21	15.03	±0.13	($n = 27$)				
	Melilite	#5	7.58	±0.08	0.91	±0.18	15.40	±0.11					
	Hibonite	#1	32.3	±0.5	−0.1	±1.9	3.8	±0.9					
	Hibonite	#2	31.6	±0.5	2.0	±1.9	5.2	±0.9	Hibonite	−0.8	±2.3	17.4	±3.4
	Hibonite	#3	32.5	±0.5	1.1	±2.3	3.4	±1.1	($n = 3$)				
	Hibonite	#4	28.3	±0.5	0.8	±2.3	3.7	±1.1					
	Hibonite	#5[d]	24.2	±0.6	0.8	±1.4	16.3	±1.0					
	Hibonite	#6[d]	35.9	±0.8	0.6	±1.6	18.3	±1.1					
	$(^{26}Al/^{27}Al)_0$	$(3.1 \pm 1.6) \times 10^{-6}$											
	$\delta^{26}Mg_0$	0.60 ± 0.10											
BG82DH8	Ca-rich forsterite	#1	0.0134	±0.0004	−0.30	±0.14	28.66	±0.15	Brigham (1990)				
	Ca-rich forsterite	#2	0.0238	±0.0008	−0.29	±0.14	26.95	±0.15					
	Spinel	#1	2.85	±0.03	0.06	±0.18	39.61	±0.16					
	Spinel	#2	2.54	±0.03	−0.03	±0.16	33.53	±0.16	Spinel	−1.7	±1.9	34.1	±6.2
	Spinel	#3	2.90	±0.03	0.03	±0.15	37.79	±0.16	($n = 10$)				
	Spinel	#4	3.13	±0.03	−0.10	±0.14	38.12	±0.16					
	Fassaite	#1	3.00	±0.03	−0.21	±0.15	33.66	±0.34					
	Fassaite	#2	2.68	±0.03	−0.11	±0.15	32.95	±0.34	Fassaite	−1.7	±1.7	30.4	±1.1
	Fassaite	#3	3.01	±0.03	−0.15	±0.16	33.10	±0.34	($n = 3$)				
	Fassaite	#4	2.92	±0.03	−0.27	±0.15	32.68	±0.34					
	Melilite	#1	3.21	±0.04	−0.09	±0.17	34.62	±0.11					
	Hibonite	#1	35.0	±0.5	−0.6	±2.1	40.4	±1.0					
	Hibonite	#2	40.6	±0.6	−0.2	±1.9	40.7	±0.9					
	Hibonite	#3	308.0	±4.8	7.3	±4.5	37.9	±2.2					
	Hibonite	#4	127.3	±1.7	3.6	±2.6	39.3	±1.3					
	Anorthite	#1	7788	±261	2.4	±18.0	14.4	±8.3	Anorthite	−16.6	±22.5	40.3	±15.9
	Anorthite	#2	8479	±508	−5.2	±17.7	22.2	±8.2	($n = 3$)				
	$(^{26}Al/^{27}Al)_0$	$(3.7 \pm 1.5) \times 10^{-6}$											
	$\delta^{26}Mg_0$	-0.20 ± 0.05											

(*continued on next page*)

Table 1 (*continued*)

Inclusion	This study								Previously reported data				
	Mineral	Spot#	$^{27}Al/^{24}Mg$	$2\sigma_m$ [a]	$\delta^{26}Mg^*$	$2\sigma_m$	F_{Mg} [b]	$2\sigma_m$		$\delta^{26}Mg^*$	2σ [c]	F_{Mg}	2σ
C1	Spinel	#1	2.50	±0.03	−0.17	±0.15	31.33	±0.16	Esat et al. (1978)				
	Spinel	#2	2.52	±0.03	−0.05	±0.14	30.82	±0.15	Spinel	−1.7	±0.8	30.3	±1.6
	Spinel	#3	2.71	±0.03	0.04	±0.20	32.16	±0.17	($n = 2$)				
	Fassaite	#1	1.52	±0.02	−0.17	±0.12	32.79	±0.34					
	Fassaite	#2	1.52	±0.02	−0.26	±0.12	32.43	±0.34	Fassaite	−1.6	±0.7	29.8	±1.2
	Fassaite	#3	2.40	±0.03	−0.21	±0.12	32.38	±0.34	($n = 3$)				
	Melilite	#1	1.91	±0.03	−0.14	±0.15	32.81	±0.11					
	Melilite	#2	2.29	±0.03	−0.03	±0.17	32.60	±0.11	Melilite	−1.4	±0.4	30.3	±3.0
	Anorthite	#1	206.1	±12.0	4.3	±3.2	30.1	±1.6	($n = 3$)				
	Anorthite	#2	213.6	±12.1	4.0	±3.6	30.6	±1.8					
	Anorthite	#3	144.2	±11.1	1.0	±3.4	22.9	±1.7	Anorthite	1.7	±2.6	18.7	±18.0
	Anorthite	#4	276.4	±13.3	2.5	±3.6	29.9	±1.8	($n = 8$)				
	Anorthite	#5	535.1	±19.8	1.0	±4.9	29.4	±2.4					
	$(^{26}Al/^{27}Al)_0$	$(2.2 \pm 1.1) \times 10^{-6}$											
	$\delta^{26}Mg_0$	-0.18 ± 0.05											
EK1-4-1	Spinel	#1	2.43	±0.03	−1.88	±0.14	21.51	±0.16	Wasserburg et al. (1977)				
	Spinel	#2	2.58	±0.03	−1.77	±0.17	24.95	±0.16	Spinel	−3.9	±0.5	20.7–22.0	
	Spinel	#3	2.63	±0.03	−1.79	±0.18	23.35	±0.16		−2.9	±0.8	16.6–21.8	
	Fassaite	#1	1.78	±0.02	−1.96	±0.13	22.17	±0.34	Fassaite	−3.6	±0.3	20.0–21.6	
	Fassaite	#2	1.77	±0.02	−1.91	±0.13	22.64	±0.34					
	$(^{26}Al/^{27}Al)_0$	$(2.3 \pm 2.4) \times 10^{-5}$; upper limit 4.7×10^{-5}											
	$\delta^{26}Mg_0$	-2.23 ± 0.37											
CG-14	Ca-rich forsterite	#1	0.0019	±0.0001	−0.45	±0.14	17.55	±0.15	Clayton et al. (1984)				
	Ca-rich forsterite	#2	0.0016	±0.0001	−0.38	±0.15	20.19	±0.15	Ca-rich forsterite	−1.5	±3.1	18.5	±2.0
	Ca-rich forsterite	#3	0.0018	±0.0001	−0.45	±0.14	18.29	±0.15	($n = 3$)				
	Fassaite	#1	1.14	±0.01	−0.30	±0.12	24.57	±0.34	Fassaite	−0.9	±0.5	18.1	±2.1
	Fassaite	#2	1.45	±0.02	−0.25	±0.14	24.63	±0.34	($n = 2$)				
	Fassaite	#3	1.45	±0.02	−0.29	±0.12	24.36	±0.34	Spinel	−0.9	±3.0	18.3	±2.7
	$(^{26}Al/^{27}Al)_0$	$(1.5 \pm 1.1) \times 10^{-5}$							($n = 4$)				
	$\delta^{26}Mg_0$	-0.42 ± 0.08											
TE	Ca-rich forsterite	#1	0.0024	±0.0003	−0.04	±0.14	12.68	±0.15	Clayton et al. (1984)				
	Ca-rich forsterite	#2	0.0030	±0.0001	−0.04	±0.14	12.91	±0.15	Ca-rich forsterite	0.5	±3.4	12.9	±1.6
	Ca-rich forsterite	#3	0.0016	±0.0001	−0.06	±0.14	13.30	±0.15	($n = 4$)				
	Fassaite	#1	1.79	±0.02	0.61	±0.12	15.89	±0.34	Spinel	−0.8	±1.6	12.9	±0.4
	Fassaite	#2	1.71	±0.02	0.63	±0.11	16.31	±0.34	($n = 2$)				
	$(^{26}Al/^{27}Al)_0$	$(5.3 \pm 0.9) \times 10^{-5}$							$(^{26}Al/^{27}Al)_0$	$\sim 4.7 \times 10^{-5}$ (El Goresy et al., 1991)			
	$\delta^{26}Mg_0$	-0.05 ± 0.08											

[a] 2 Standard error of mean, including internal error of each analysis and reproducibility of standard measurements.
[b] Intrinsic mass fractionation, given by $\delta^{25}Mg_{sample} - \delta^{25}Mg_{standard}$.
[c] 2 Standard deviation of the literature data.
[d] Measured in section *AXCAI 2571*.

Magnesium in hibonite intergrown with spinel in the periphery of *AXCAI 2271* is less fractionated (F_{Mg} ~3–5‰/amu) than that in hibonite in *AXCAI 2571* (F_{Mg} ~16–18‰/amu) (Table 1, Fig. 8). The highly fractionated magnesium isotopic compositions in *AXCAI 2571* are consistent with the previously reported values of hibonite in sections *AXCAI 2571* and *2771* by Srinivasan et al. (2000). The internal aluminum-magnesium isochron defined by spinel, melilite, and hibonite has $(^{26}Al/^{27}Al)_0$ of $(3.1 \pm 1.6) \times 10^{-6}$ and $\delta^{26}Mg_0$ of 0.60 ± 0.10‰ (Fig. 2).

3.2. BG82DH8

BG82DH8 is a Type B FUN CAI identified by Papanastassiou and Brigham (1989). The CAI consists of two lithologies – Type B and forsterite-rich Type B (FoB) (Fig. 1b–d). In the Type B lithology, fassaite (in wt%, TiO_2: 3.6–16.9, Al_2O_3: 10.8–25.1) and spinel are the dominant minerals; anorthite and melilite ($Åk_{21-44}$) are less abundant. The peripheral part of the Type B lithology contains lath-like hibonite (in wt%, TiO_2: 1.6–6.8, MgO: 1.0–3.1) intergrown with spinel (Figs. S2i–l). The FoB lithology is composed of coarse-grained calcium-rich forsterite (1.6–1.9 wt% CaO), fassaite (in wt%, TiO_2: 7.4–18.8, Al_2O_3: 15.8–20.2), spinel enriched in FeO, and abundant secondary minerals, including nepheline, ferroan olivine (Fa_{31-35}), salite-hedenbergite pyroxenes, and andradite (Krot et al., 2014). Textural relationships between the lithologies are not clear (Figs. 1c, S2a).

Magnesium isotopes were measured in forsterite from the FoB lithology, and fassaite, spinel, melilite, and hibonite from the Type B lithology. *BG82DH8* has the most fractionated magnesium-isotope composition (F_{Mg} ~14–41‰/amu; Table 1) among the FUN CAIs studied; these values are comparable to the previously reported data (Brigham, 1990). Hibonite and minerals with low $^{27}Al/^{24}Mg$ ratios (calcium-rich forsterite, fassaite, spinel, and melilite) define an internal aluminum-magnesium isochron with $(^{26}Al/^{27}Al)_0$ of $(3.7 \pm 1.5) \times 10^{-6}$ and $\delta^{26}Mg_0$ of -0.20 ± 0.05‰ (Fig. 3a). Two analyses of anorthite have very high $^{27}Al/^{24}Mg$ ratios (~8,000) and show no resolvable excess of ^{26}Mg (Fig. 2b); these data were excluded from the internal isochron because of the possible disturbance of the aluminum-magnesium isotope systematics due to the observed cracks and holes in these spots (Fig. S2m,n).

3.3. C1

C1 is a Type B FUN CAI described originally by Clayton and Mayeda (1977) and Wasserburg et al. (1977). We studied three polymineralic fragments of *C1* (Figs. 1e, S3). The fragments consist of fassaite (in wt%, TiO_2: 3–8, Al_2O_3: 12.8–22.9), anorthite, melilite ($Åk_{73-80}$), and spinel. Melilite is extensively replaced by grossular, monticellite,

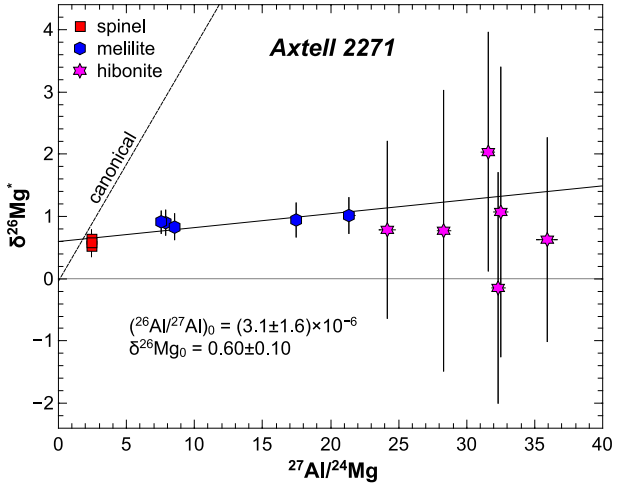

Fig. 2. Aluminum-magnesium evolutionary diagram of *Axtell 2271*. Data for spinel, melilite, and hibonite define a regression line with $(^{26}Al/^{27}Al)_0$ of $(3.1 \pm 1.6) \times 10^{-6}$ and an intercept of 0.60 ± 0.10‰. Here and in Figs. 3–8, Isoplot Model 1 (Ludwig, 2003) was used to fit isochrons; all errors are 2σ and the canonical $(^{26}Al/^{27}Al)_0$ of 5.23×10^{-5} (Jacobsen et al., 2008a) is shown for reference.

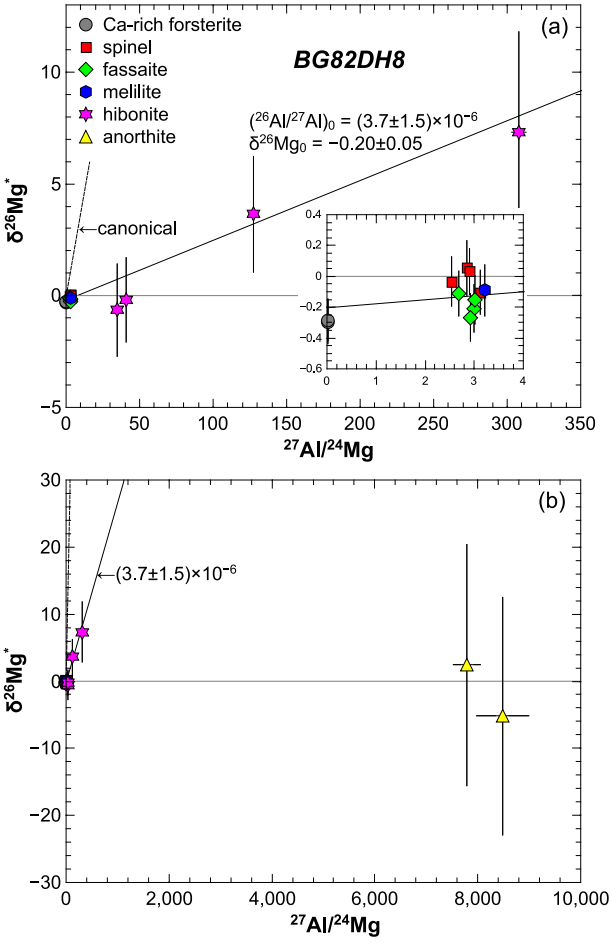

Fig. 3. Aluminum-magnesium evolutionary diagram of *BG82DH8*. (a) Data for hibonite, melilite, spinel, fassaite, and Ca-rich forsterite define an isochron with $(^{26}Al/^{27}Al)_0$ of $(3.7 \pm 1.5) \times 10^{-6}$ and an intercept of -0.20 ± 0.05‰. (b) Anorthite has an extremely high $^{27}Al/^{24}Mg$ ratio and shows no resolvable excess of ^{26}Mg.

titanium-poor aluminum-diopside, and forsterite; anorthite is partly replaced by nepheline, sodalite, and ferroan olivine (Fa_{18-21}) (Krot et al., 2014).

Magnesium isotopes were measured in anorthite, melilite, fassaite, and spinel. Magnesium in fassaite, melilite, and spinel shows a similar degree of fractionation (F_{Mg} ~ 31–33‰/amu); magnesium in anorthite is less fractionated (F_{Mg} ~23–31‰/amu; Table 1). Esat et al. (1978) also reported variable and less-fractionated magnesium isotopic compositions of anorthite (F_{Mg} ~3–31‰/amu) compared to other minerals in *C1*. Fassaite, spinel, melilite, and anorthite define an internal isochron with $(^{26}Al/^{27}Al)_0$ of $(2.2 \pm 1.1) \times 10^{-6}$ and $\delta^{26}Mg_0$ of -0.18 ± 0.05‰ (Fig. 4). The $\delta^{26}Mg_0$ of *C1* in this study is resolvable from zero but less negative than ~−1.8‰ reported by Esat et al. (1978), possibly due to inappropriate fractionation law (power law) with β of 0.500 (Davis et al., 2015). One spot in anorthite (#5 in Table 1) having a crack and located close to an alteration area (Fig. S3c) shows no resolvable excess of ^{26}Mg; this spot was excluded from the internal isochron. Considering that magnesium isotopic data of anorthite from Allende CAIs are often disturbed (e.g., Podosek et al., 1991; MacPherson et al., 1995), we cannot exclude the possibility that the internal isochron of *C1* defined by mostly anorthite data may not represent the initial $^{26}Al/^{27}Al$ ratio of the CAI.

3.4. EK1-4-1

EK1-4-1 is a Type B FUN CAI as described by Nagasawa et al. (1982) and studied by Clayton and Mayeda (1977) and Wasserburg et al. (1977). During these studies, it was disaggregated and nearly completely consumed. Only small polished fragments of this CAI composed of fassaite (in wt%, TiO_2: 0.67–10.7, Al_2O_3: 15.8–22.6), spinel, and rare melilite were available for our study (Figs. 1f, S4). Melilite ($Åk_{28-67}$) is replaced by grossular, monticellite, forsterite, titanium-poor aluminum-diopside, wadalite, wollastonite, nepheline, and andradite.

Magnesium isotopes were measured only in fassaite and spinel; melilite grains free of secondary minerals were too small for high-precision magnesium isotopic measurements by SIMS. Magnesium in fassaite and spinel is similarly fractionated, F_{Mg} ~22–25‰/amu (Table 1), consistent with the previously reported TIMS data (Wasserburg et al., 1977). Both minerals have negative values of $\delta^{26}Mg_0$ (~−2‰). The inferred initial $^{26}Al/^{27}Al$ ratio of $(2.3 \pm 2.4) \times 10^{-5}$ is not resolved from zero.

3.5. CG-14

CG-14 is a FoB CAI identified as a FUN inclusion based on the mass-dependent fractionations in oxygen, magnesium, and silicon isotopes, and an isotopic anomaly in magnesium (Clayton et al., 1984). Two small fragments of *CG-14* were available for our study (Fig. 1g, S5). Both fragments consist of fassaite (in wt%, TiO_2: 2.6–5.9, Al_2O_3: 10.0–18.7), calcium-rich forsterite (1.9–2.3 wt% CaO), spinel, and åkermanitic melilite ($Åk_{87-90}$) replaced by titanium-free aluminum-diopside, wadalite, wollastonite, nepheline, sodalite, and ferroan olivine. Spinel and forsterite are heterogeneously distributed in *CG-14* and both forsterite-rich and forsterite-poor lithologies can be identified. Only calcium-rich forsterite and fassaite were measured for magnesium isotopic composition.

Calcium-rich forsterite and fassaite show large F_{Mg}, ~18–20‰/amu and ~24–25‰/amu, respectively (Table 1). The F_{Mg} values of fassaite are larger than the previously reported value of ~18‰/amu (Clayton et al., 1984). The minerals define the internal isochron with $(^{26}Al/^{27}Al)_0$ of $(1.5 \pm 1.1) \times 10^{-5}$ and $\delta^{26}Mg_0$ of -0.42 ± 0.08‰ (Table 1, Fig. 6). We note that the inferred $(^{26}Al/^{27}Al)_0$ of *CG-14* is not resolvable from zero with β of 0.511 (Table 2).

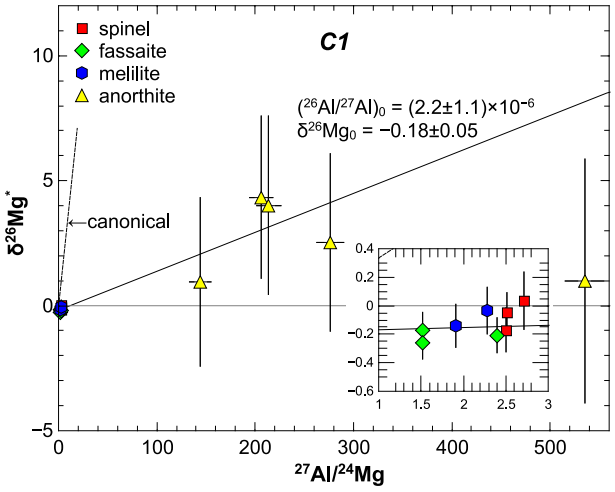

Fig. 4. Aluminum-magnesium evolutionary diagram of *C1*. Data for melilite, fassaite, spinel, and anorthite (except anorthite grain #5 on a small crack) define a regression line with a slope of $(2.2 \pm 1.1) \times 10^{-6}$ and an intercept of -0.18 ± 0.05‰.

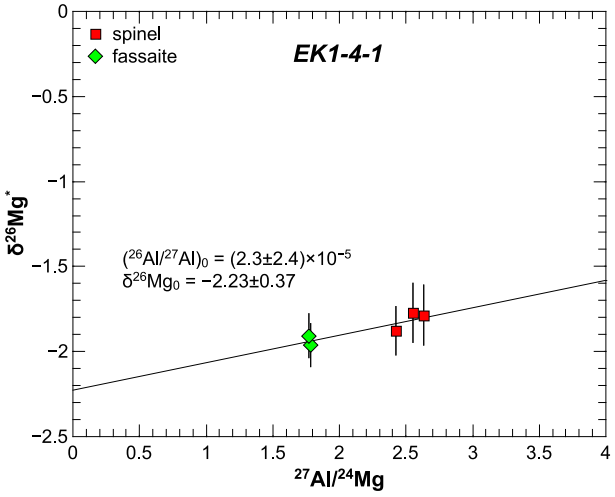

Fig. 5. Aluminum-magnesium evolutionary diagram of *EK1-4-1*. The inferred isochron, $(^{26}Al/^{27}Al)_0 = (2.3 \pm 2.4) \times 10^{-5}$, is not resolved from zero, but has a large negative intercept of -2.23 ± 0.37‰.

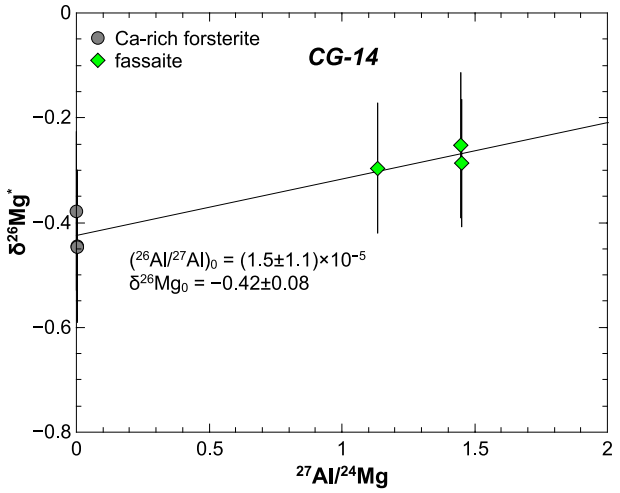

Fig. 6. Aluminum-magnesium evolutionary diagram of *CG-14*. Data for fassaite and forsterite define an isochron with a slope of $(1.5 \pm 1.1) \times 10^{-5}$ and a negative intercept of -0.42 ± 0.08‰.

3.6. TE

TE is a FoB CAI originally described by Dominik et al. (1978) and identified as a FUN inclusion based on oxygen and magnesium isotopic compositions by Clayton et al. (1984). However, subsequent studies by Zinner et al. (1989) and El Goresy et al. (1991) classified TE as an F CAI based on its normal calcium and titanium isotopic compositions (Jungck et al., 1984; Niederer et al., 1985). Only small fragments of *TE* composed of fassaite (in wt %, TiO_2: 2.2-4.5, Al_2O_3: 11.4–21.6), calcium-rich forsterite (1.3–1.7 wt% CaO), melilite ($Åk_{59-93}$), and spinel were available for our study (Figs. 1h, S6). Calcium-rich forsterite encloses tiny spinel grains (Fig. 1h). Melilite is extensively replaced by titanium-poor aluminum-diopside, grossular, monticellite, wadalite, and wollastonite, and was not measured for magnesium isotopic compositions. Spinel grains were too small for high-precision magnesium isotopic measurements.

Calcium-rich forsterite and fassaite show large F_{Mg} of ~13‰/amu and ~16‰/amu, respectively, confirming the results of previous studies (Clayton et al., 1984; Zinner et al., 1989; El Goresy et al., 1991). These minerals define an internal isochron with $(^{26}Al/^{27}Al)_0$ of $(5.3 \pm 0.9) \times 10^{-5}$ and $\delta^{26}Mg_0$ of -0.05 ± 0.08‰ (Table 1, Fig. 7). The inferred $(^{26}Al/^{27}Al)_0$ is consistent with the previously reported value for *TE* of $\sim 4.7 \times 10^{-5}$ based on magnesium-isotope measurements of hibonite (El Goresy et al., 1991).

4. DISCUSSION

4.1. Brief summary of aluminum-magnesium isotope systematics of FUN CAIs

Our *in situ* magnesium isotopic measurements of individual minerals in FUN CAIs confirm the highly fractionated magnesium isotopic compositions measured

Table 2
Internal isochron regressions of FUN CAIs showing the effect of corrections for mass-dependent fractionation using the exponential law with different exponents (β).

	β = 0.511			β = 0.5128			β = 0.514		
	$(^{26}Al/^{27}Al)_0$	$\delta^{26}Mg_0$	MSWD[1]	$(^{26}Al/^{27}Al)_0$	$\delta^{26}Mg_0$	MSWD[1]	$(^{26}Al/^{27}Al)_0$	$\delta^{26}Mg_0$	MSWD[1]
Axtell 2271	$(3.1 \pm 1.6) \times 10^{-6}$	0.49 ± 0.10	0.93	$(3.1 \pm 1.6) \times 10^{-6}$	0.60 ± 0.10	0.96	$(3.1 \pm 1.6) \times 10^{-6}$	0.67 ± 0.10	0.99
BG82DH8	$(3.5 \pm 1.5) \times 10^{-6}$	-0.43 ± 0.05	1.3	$(3.7 \pm 1.5) \times 10^{-6}$	-0.20 ± 0.05	1.7	$(3.9 \pm 2.4) \times 10^{-6}$	-0.06 ± 0.08	2.1
CI	$(2.2 \pm 1.1) \times 10^{-6}$	-0.40 ± 0.05	1.3	$(2.2 \pm 1.1) \times 10^{-6}$	-0.18 ± 0.05	1.3	$(2.2 \pm 1.1) \times 10^{-6}$	-0.04 ± 0.05	1.3
EKI-4-1	$(2.1 \pm 2.4) \times 10^{-5}$	-2.36 ± 0.37	0.22	$(2.3 \pm 2.4) \times 10^{-5}$	-2.23 ± 0.37	0.33	$(2.3 \pm 2.4) \times 10^{-5}$	-2.13 ± 0.37	0.41
CG-14	$(1.1 \pm 1.1) \times 10^{-5}$	-0.55 ± 0.08	0.11	$(1.5 \pm 1.1) \times 10^{-5}$	-0.42 ± 0.08	0.18	$(1.8 \pm 1.1) \times 10^{-5}$	-0.34 ± 0.08	0.23
TE	$(5.1 \pm 0.9) \times 10^{-5}$	-0.14 ± 0.08	0.13	$(5.3 \pm 0.9) \times 10^{-5}$	-0.05 ± 0.08	0.15	$(5.4 \pm 0.9) \times 10^{-5}$	0.01 ± 0.08	0.16

[1] Mean square weighted deviations of the regression lines using Isoplot Model 1 (Ludwig, 2003).

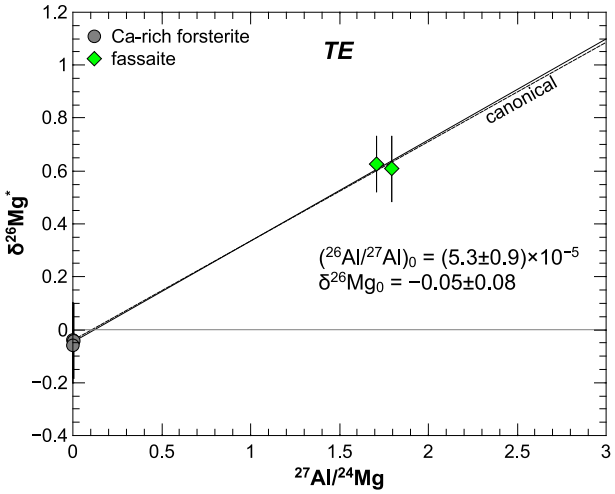

Fig. 7. Aluminum-magnesium evolutionary diagram of *TE*. The inferred initial $^{26}Al/^{27}Al$ ratio of $(5.3 \pm 0.9) \times 10^{-5}$ is indistinguishable from the canonical value and consistent with the previously reported value in hibonite ($\sim 4.7 \times 10^{-5}$) by El Goresy et al. (1991).

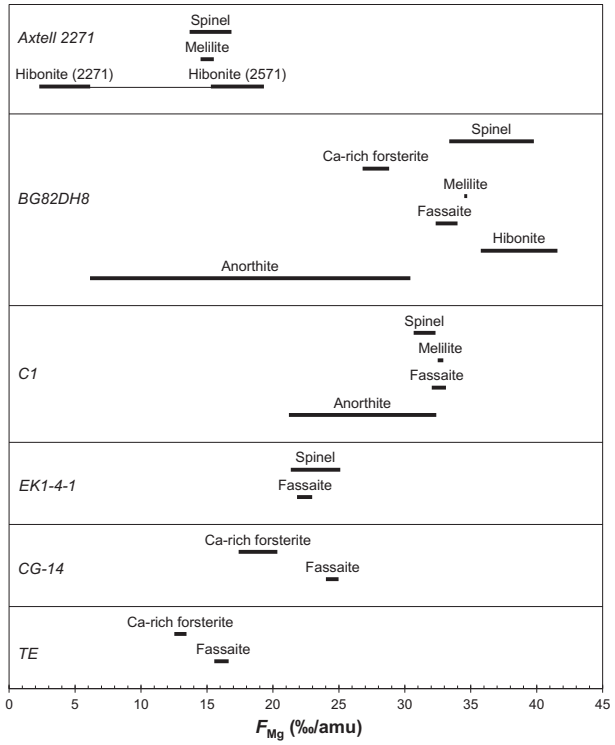

Fig. 8. The intrinsic magnesium-isotope fractionation effects (F_{Mg}) of individual minerals in six FUN CAIs. Hibonite grains measured in sections *AXCAI 2271* and *2571* show distinct F_{Mg} values, possibly due to partial recondensation (back reaction) of magnesium at the last stage of solidification resulting in a decrease of F_{Mg} in some hibonite grains. Relatively low F_{Mg} and its wide range in anorthite in *BG82DH8* and *C1* may have resulted from magnesium-isotope disturbance during thermal metamorphism on the Allende parent body.

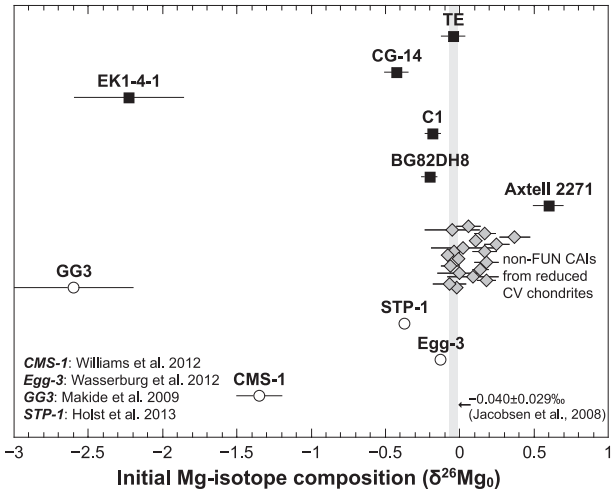

Fig. 9. Initial magnesium-isotope compositions ($\delta^{26}Mg_0$) of non-FUN CAIs from reduced CV3 chondrites and FUN CAIs. Data for FUN CAIs from this study and the literature data are shown by filled squares and open circles, respectively. FUN CAIs have $\delta^{26}Mg_0$ values distinctly different from those yielded by internal isochrons of non-FUN CAIs (diamond; data from Kita et al., 2012; MacPherson et al., 2012, and Mishra and Chaussidon, 2014) and by a bulk model isochron of non-FUN CAIs from the oxidized CV chondrites Allende (-0.040 ± 0.029‰ indicated by a gray line; Jacobsen et al., 2008a). Although the use of different β values (0.5128 for six FUN CAIs in this study, 0.514 for *GG3* (Makide et al., 2009) and *CMS-1* (Williams et al., 2012), and 0.511 for the others) can change $\delta^{26}Mg_0$ values by up to several tenths of a permil, it cannot explain the large variation in negative $\delta^{26}Mg_0$ values of FUN CAIs. These observations provide evidence for magnesium-isotope heterogeneity in the protoplanetary disk region where FUN CAIs formed.

previously (Table 1, Fig. 8; Wasserburg et al., 1977; Esat et al., 1978; Clayton et al., 1984; Zinner et al., 1989; Brigham, 1990; El Goresy et al., 1991; Srinivasan et al., 2000). In Figs. 9 and 10, we plot the $\delta^{26}Mg_0$ and $(^{26}Al/^{27}Al)_0$ values, respectively, in all known FUN CAIs. There are significant variations in $\delta^{26}Mg_0$ values among them. Four out of the six FUN CAIs studied, except *Axtell 2271* and *TE*, show more negative $\delta^{26}Mg_0$ values than non-FUN CAIs (Fig. 9). The deficit of $\delta^{26}Mg_0$ is most plausibly due to an intrinsic isotope anomaly in either the $^{25}Mg/^{24}Mg$ or $^{26}Mg/^{24}Mg$ ratio relative to the terrestrial values (Wasserburg et al., 2012). If the $^{25}Mg/^{24}Mg$ ratio is anomalous, the magnesium isotopic fractionation (F_{Mg}) in FUN CAIs studied includes this anomaly. However, the observed anomalies in magnesium ($\delta^{26}Mg_0$ values) are much smaller than the observed $\delta^{25}Mg$ values, and thus, can contribute only small changes in the F_{Mg} values. For example, the $\delta^{26}Mg_0$ value of −2.23‰ in *EK1-4-1* is equivalent to a $^{25}Mg/^{24}Mg$ shift of +1.14‰ from the terrestrial value and thus is significantly smaller than the observed magnesium isotopic fractionation (~22–25‰). Since it is impossible to determine which of the magnesium isotope ratios is anomalous, we assume the mass-independent shift occurs only in $^{26}Mg/^{24}Mg$.

Contrary to the view that FUN CAIs formed with almost no ^{26}Al (e.g., MacPherson et al., 1995), *BG82DH8*

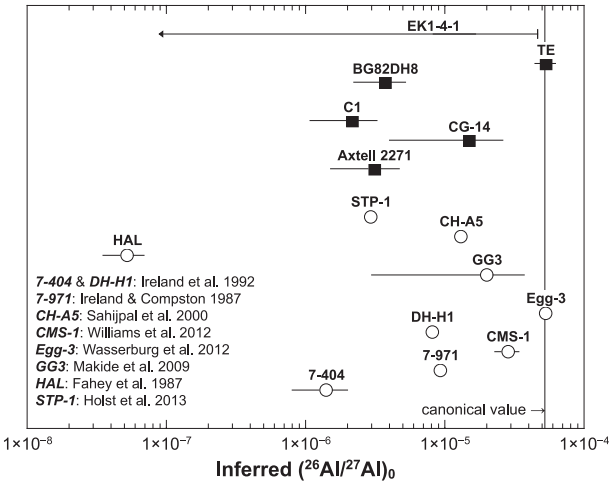

Fig. 10. Inferred initial $^{26}Al/^{27}Al$ ratios in FUN CAIs. Data from this study and the literature data are shown by filled squares and open circles, respectively. *EK1-4-1* is shown with an arrow because of its unresolvable $(^{26}Al/^{27}Al)_0$ from zero. Most FUN CAIs show resolvable ^{26}Mg excesses corresponding to inferred $(^{26}Al/^{27}Al)_0$ ranging from $\sim 5 \times 10^{-8}$ to $\sim 5 \times 10^{-5}$. A linear mass fractionation law was used to reduce data for *7–404*, *DH-H1*, *7–971*, *CH-A5*, and *HAL*. An exponential law with an exponent β of 0.5128 was used to reduce data for six FUN CAIs in this study; 0.514 for *CMS-1* and *GG3*, and 0.511 for *Egg-3* and *STP-1* were used. Although the lack of raw data in literature does not allow us to compare the effects of different laws and β values on $(^{26}Al/^{27}Al)_0$, the difference is probably not significant based on our results (Table 2). Thus, the large variability in $(^{26}Al/^{27}Al)_0$ among FUN CAIs exists in any fractionation law. The canonical $(^{26}Al/^{27}Al)_0$ of 5.23×10^{-5} (Jacobsen et al., 2008a) is shown for reference.

and *TE* show clearly resolvable excesses of radiogenic ^{26}Mg and well-defined internal ^{26}Al-^{26}Mg isochrons; *Axtell 2271*, *C1*, and *CG-14* have marginally resolvable ^{26}Al-^{26}Mg isochrons. The inferred $(^{26}Al/^{27}Al)_0$ values of FUN CAIs range from $\sim 5 \times 10^{-8}$ to nearly the canonical value (Fig. 10). Below we discuss the significance of these results for understanding the origin of FUN CAIs and the distribution of ^{26}Al and magnesium isotopes in the solar nebula.

4.1.1. Mass fractionation correction

Since FUN CAIs exhibit large magnesium-isotope fractionation effects, it is particularly important to correct these effects appropriately to obtain accurate $\delta^{26}Mg^*$ values. In 1970s, magnesium-isotope fractionations of data from FUN CAIs were corrected using a power law with β of 0.5 (Esat et al., 1978; Lee et al., 1976; Wasserburg et al., 1977; see Davis et al., 2015). After Russell et al. (1978), the exponential law has been widely used to correct mass fractionation effects. However, there is no agreement on the value of an exponent β in the exponential law to describe the mass-dependent fractionation experienced by CAIs (e.g., Young et al., 2002; Davis et al., 2005, 2015; McKeegan et al., 2005; Wasserburg et al., 2012). In this study, we chose a β value of 0.5128 inferred from vacuum evaporation experiments of CAI-like melts (Davis et al., 2015), because FUN CAIs appear to have experienced extensive melt evaporation under low gas pressure (Mendybaev et al., 2013, 2017). In contrast, most magnesium isotopic data for CAIs collected by MC-ICP-MS were treated with the exponential law with a β value of 0.511 (e.g., Jacobsen et al., 2008a; Larsen et al., 2011; Wasserburg et al., 2012). Using the criterion that the choice of β should be based on obtaining an isochron with MSWD (mean square weighted deviation) close to unity, Wasserburg et al. (2012) demonstrated that only β values between 0.509 and 0.513 yield good ^{26}Al-^{26}Mg isochrons for CAIs. To assess the uncertainty caused by the choice of β, we compare the effects of β values of 0.511, 0.5128, and 0.514 used to determine $\delta^{26}Mg_0$ and $(^{26}Al/^{27}Al)_0$ in individual FUN CAIs (Table 2).

If a CAI has homogeneous magnesium isotopic composition, changing β moves all data points on an Al-Mg evolution diagram up and down the same amount, resulting in a systematical increase of $\delta^{26}Mg_0$ values with increase of β values (refer to Eq. (9)). The changes of $\delta^{26}Mg_0$ values in this study range from ~0.15‰ to ~0.37‰ and largely depend on the F_{Mg} values of individual CAIs. Four out of the six FUN CAIs studied here have resolvable deficits in $\delta^{26}Mg_0$ with β value of 0.5128, compared to five and three of six with β values of 0.511 and 0.514, respectively. The overall range of $\delta^{26}Mg_0$ values among FUN CAIs is similar (~2.8‰), irrespective of β values, and thus represents the possible degree of magnesium-isotope heterogeneity recorded by FUN CAIs.

The inferred initial $^{26}Al/^{27}Al$ ratios do not change with β in a systematic way because they largely depend on magnesium isotopic compositions and $^{27}Al/^{24}Mg$ ratios of individual minerals rather than β values. Although $(^{26}Al/^{27}Al)_0$ values slightly change with different β values, the observation that FUN CAIs show a large range in $(^{26}Al/^{27}Al)_0$ from nearly the canonical value to $\sim 5 \times 10^{-8}$ remains valid (Fig. 10).

4.2. Magnesium fractionation effects in FUN CAIs

All of the minerals in the FUN CAIs show evidence for mass-dependent magnesium isotopic fractionation (Table 1). This observation together with the mineralogy, petrography, and oxygen isotopic compositions (Krot et al., 2014) suggests FUN CAIs were once completely molten and experienced evaporation before and during crystallization. To test whether mass-dependent fractionation effects in magnesium, silicon, and oxygen in FUN CAIs resulted from melt-evaporation, Mendybaev et al. (2013, 2017) conducted a series of evaporation experiments of magnesium- and silicon-rich melts at 1900 °C in vacuum (total pressure $< 10^{-9}$ atm). They found that (1) the fractionation of 6–30‰/amu in magnesium and silicon observed in FUN CAIs could have been produced by evaporation of 30–80% of the magnesium and silicon from the precursor melts and (2) the chemical and isotopic compositions of *C1* are consistent with evaporation from a molten precursor with a bulk composition close to that predicted for a condensate from a solar composition gas. The inferred *in vacuo* melt-evaporation to explain the large mass fractionation in FUN CAIs is supported by simulations

of oxygen isotopic fractionation during evaporation/condensation (Nagahara and Ozawa, 2012). These authors concluded that the large oxygen isotopic fractionation observed in FUN CAIs requires near vacuum condition to efficiently separate gas from melt during evaporation. Similarly large mass-dependent fractionation in magnesium was also produced in evaporation experiments of a Type B CAI-like composition melt at P_{H_2} of $\sim 2 \times 10^{-4}$ bar at 1500 °C (Richter et al., 2002). These experiments showed that the evaporation rate of magnesium from a melt is much faster in a hydrogen-rich gas than in vacuum, and indicated that temperature, total gas pressure, duration of evaporation, and composition of a precursor all play a role affecting the mass-dependent fractionation effects observed in FUN CAIs.

If FUN CAIs crystallized during melt-evaporation, an increase in the extent of mass-dependent fractionation of magnesium isotopes would be expected to follow the crystallization sequence. Based on mineralogical observations and melt crystallization experiments (Stolper, 1982), the general crystallization sequence of the FUN CAIs studied here is spinel → calcium-rich forsterite (only in FoB FUN CAIs) → melilite → fassaite + anorthite; in some FUN CAIs hibonite in the peripheral portions appears to have crystallized last. There is general consistency between the inferred crystallization sequence and the degree of magnesium-isotope fractionation in FUN CAIs, as seen in *Axtell 2271*, *CG-14*, and *TE* (Fig. 8). Clear exceptions are calcium-rich forsterite in *BG82DH8*, and anorthite in *BG82DH8* and *C1* (Fig. 8).

BG82DH8 consists of two lithologies – FoB and Type B; the textural relationship between the lithologies is unclear (Krot et al., 2014). Since the magnesium isotopic compositions of forsterite and spinel were measured in different lithologies, we cannot exclude the possibility that the lithologies experienced different evaporation histories prior to aggregation into the present object. However, we note that these lithologies likely formed simultaneously because all minerals, except anorthite, in *BG82DH8* plot on a single Al-Mg regression line (Fig. 3). Two anorthite grains measured in *BG82DH8* and one anorthite in *C1* contain a small hole or a crack (Figs. S2m,n, S3c). The holes and cracks could facilitate the exchange magnesium isotopes with an asteroidal fluid during metamorphism on the Allende parent body (e.g., Podosek et al., 1991; MacPherson et al., 1995; Kita et al., 2012).

It should be noted that the magnesium-isotope fractionation (F_{Mg}) of ~3–5‰/amu in hibonite in section *AXCAI 2271* is much less than the ~14–17‰/amu value in spinel and melilite in the same section, ~16–18‰/amu in hibonite in section *2571* (Table 1, Fig. 8), and ~16–19‰/amu in section *2771* measured by Srinivasan et al. (2000). A similarly wide range of magnesium-isotope fractionation in different hibonite grains was observed in the Allende FUN CAI *STP-1* (Holst et al., 2013). To explain these observations, four possibilities are considered: (1) late accretion of exotic hibonite grains; (2) a late heating event that melted some of the hibonite in the peripheral portions of the CAIs, followed by magnesium-isotope exchange with a gas of solar composition; (3) partial recondensation (back-reaction) of magnesium from the previously evaporated gas at relatively high total pressure; and (4) partial re-equilibration of magnesium isotopes via diffusive exchange in a gaseous reservoir and/or on the CV chondrite body.

We consider each of the four scenarios in turn.

1. The hibonite grains in *Axtell 2271* measured for magnesium isotopes are located in peripheral portions of sections *AXCAI 2271* and *2771*. The texture and mineral chemistry of hibonite grains from two sections are almost identical (Srinivasan et al., 2000; Krot et al., 2014), implying their cogenetic origin; thus, late accretion of some exotic hibonite grains is unlikely.
2. Melting only the periphery of the CAIs without melting melilite inside the CAIs seems unlikely because of the low melting temperature of melilite compared to hibonite and spinel (Beckett and Stolper, 1994); thus, gas–melt exchange can be excluded.
3. *Axtell 2271* and *STP-1* show less magnesium isotopic fractionation than other FUN CAIs (Brigham, 1990; Thrane et al., 2008; Makide et al., 2009; Holst et al., 2013; this study), suggesting they may have experienced melting and evaporation at higher ambient gas pressure than other FUN CAIs. This scenario provides greater opportunity to recondense magnesium from the surrounding gas into hibonite during the last stage of melt-solidification and appears consistent with the variable degree of oxygen isotopic fractionation of minerals in some FUN CAIs that is otherwise inconsistent with the crystallization sequence (Krot et al., 2014).
4. It is unlikely that the magnesium isotopes in only some hibonite grains in the peripheral portions of the CAIs were selectively reequilibrated by diffusive exchange; however, we cannot rule out the possibility of partial magnesium isotopic exchange for some hibonite grains.

4.3. Heterogeneity of initial $^{26}Mg/^{24}Mg$ ratio in the early Solar System

Assuming a homogeneous distribution of magnesium isotopes, an $^{26}Al/^{27}Al$ ratio at the canonical level of 5.23×10^{-5} in the early Solar System and a solar $^{27}Al/^{24}Mg$ ratio of 0.101 (Palme et al., 2014), the initial $^{26}Mg/^{24}Mg$ ratio in the Solar System should have a value of −0.038‰, representing the intercept of the canonical aluminum-magnesium isochron with the solar $^{27}Al/^{24}Mg$ ratio (Larsen et al., 2011). If CAIs formed in a reservoir isotopically identical to the bulk Solar System, their initial $^{26}Mg/^{24}Mg$ should be also −0.038‰. Jacobsen et al. (2008a) reported a $\delta^{26}Mg_0$ of -0.040 ± 0.029‰ for the Allende CAIs, consistent with this value. In contrast, Larsen et al. (2011) obtained more precise $\delta^{26}Mg_0$ of -0.0159 ± 0.0014‰ from a combined model isochron of CAIs and AOAs from the reduced CV chondrite Efremovka. This value is significantly higher than the predicted solar $\delta^{26}Mg_0$ value but is not resolved from the value reported by Jacobsen et al. (2008a). Wasserburg et al. (2012) pointed out that the elevated $\delta^{26}Mg_0$ value obtained by Larsen et al. (2011) could result from their approach of

combining data for CAIs and AOAs to define a single aluminum–magnesium isochron; AOAs may have postdated the formation of CAIs and the two groups of refractory inclusions would not form a single population [note that this conclusion is inconsistent with the inferred $(^{26}Al/^{27}Al)_0$ in FoB non-FUN CAIs, which is indistinguishable from the canonical value reported by Bullock et al. (2017), because FoB CAIs postdate formation of AOAs]. Wasserburg et al. (2012) showed that the isochron regressed through the CAI data from Larsen et al. (2011) alone gives a $\delta^{26}Mg_0$ value of $-0.030 \pm 0.040‰$, consistent with the solar value. To obtain an accurate initial $^{26}Mg/^{24}Mg$ ratio for the region where a CAI formed, they defined an internal isochron for the Allende CAI *Egg-3* corresponding to an $(^{26}Al/^{27}Al)_0$ of $(5.27 \pm 0.18) \times 10^{-5}$ and $\delta^{26}Mg_0$ value of $-0.127 \pm 0.032‰$. Since *Egg-3* has an $(^{26}Al/^{27}Al)_0$ unresolvable from the canonical value but a significantly different $\delta^{26}Mg_0$ from the value determined by Jacobsen et al. (2008a), Wasserburg et al. (2012) concluded that magnesium-isotope heterogeneity existed in the early Solar System during CAI formation. The magnesium-isotope data for the six FUN CAIs studied here strengthen the conclusion of Wasserburg et al. (2012): four of the CAIs (*EK1-4–1*, *C1*, *BG82DH8*, and *CG-14*) show variable and, more importantly, large deficits in the initial $^{26}Mg/^{24}Mg$ ratio; the only exceptions are *Axtell 2271* and *TE* (Tables 1 and 2; Figs. 2–7 and 9).

Negative $\delta^{26}Mg_0$ values of internal isochrons have been previously reported in several other FUN CAIs: $-2.6 \pm 0.4‰$ for *Gao-Guenie (b) #3* (hereafter *GG3*) from the Gao-Guenie (b) CR2 chondrite (Makide et al., 2009), $-1.35 \pm 0.15‰$ for *CMS-1* (Williams et al., 2012), and $-0.371 \pm 0.010‰$ of *STP-1* from Allende (Holst et al., 2013) (Fig. 9). A β value of 0.514 was used to reduce the data for *GG3* and *CMS-1*, while a β value of 0.511 was used for *STP-1*. Although the use of different β values changes $\delta^{26}Mg_0$ values by up to several tenths of a permil, it cannot explain the large variation among the negative $\delta^{26}Mg_0$ values in FUN CAIs (Fig. 9).

Large deficits in $\delta^{26}Mg^*$ were also reported in some PLAty-Crystal (PLAC) and Blue AGgregate (BAG) hibonites from CM chondrites (Ireland et al., 1986; Liu et al., 2009, 2012), hibonite-bearing microspherules from CO3 and CM chondrites (Ireland et al., 1991; Russell et al., 1998), a hibonite-pyroxene spherule *86* from the ungrouped carbonaceous chondrite Acfer 094 (Sugiura and Krot, 2007), and a hibonite-grossite-rich CAI *MK #5* from the El Djouf CR chondrite (Makide et al., 2009). Some of these inclusions show large mass-dependent fractionation effects in magnesium (grain *43* and *61*; Ireland et al., 1986) or oxygen (*MUR-B1*; Liu et al., 2009), and, therefore, can be classified as FUN inclusions. Liu and McKeegan (2009) and Liu et al. (2012) considered protosolar irradiation of the isotopically normal grains as a cause of the large negative $\delta^{26}Mg^*$ values ($\geqslant -4‰$) observed in PLACs. However, this mechanism failed to produce magnesium isotopic anomalies as low as $-4‰$. We conclude that large and variable negative values of $\delta^{26}Mg_0$ in both FUN and normal refractory inclusions reflect magnesium isotopic heterogeneity in the CAI-forming region(s) of the early Solar System.

The positive intercept of the internal isochron of the CTA CAI *Axtell 2271*, ($\delta^{26}Mg_0 = 0.60 \pm 0.10‰$; Fig. 2) may reflect either the initial heterogeneity in $\delta^{26}Mg_0$ or the subsequent resetting of the aluminum-magnesium isotope systematics after decay of some ^{26}Al in the solar nebula or on the CV parent body (e.g., Simon and Young, 2011; MacPherson et al., 2012). Magnesium isotopic resetting by solid-state diffusive exchange between mineral phases on the CV parent body is unlikely because of sluggish magnesium self-diffusion in melilite (Ito and Ganguly, 2009), even at the peak metamorphic temperature (~800 K) apparently reached by Allende (Weinbruch et al., 1994; Bonal et al., 2006). Assuming ^{26}Al was homogeneously distributed in the early Solar System at the canonical level, the inferred $(^{26}Al/^{27}Al)_0$ in *Axtell 2271* [$(3.1 \pm 1.6) \times 10^{-6}$] may suggest a last melting event ~3 Ma after the crystallization of CV CAIs with the canonical $(^{26}A/^{27}Al)_0$ ratio. If *Axtell 2271* behaved as a closed system during the last melting event, the $\delta^{26}Mg_0$ value of its precursor should have been approximately $-2.3‰$ to explain the observed value of $\delta^{26}Mg_0$, $0.60 \pm 0.10‰$, in light of the bulk CAI $^{27}Al/^{24}Mg$ ratio of ~8.2 derived from the modal abundance and average chemical compositions of major mineral phases (Srinivasan et al., 2000). Alternatively, if *Axtell 2271* formed early, similar to most CAIs, but with much lower $(^{26}Al/^{27}Al)_0$ than the canonical value (see section 4.4), the positive $\delta^{26}Mg_0$ would represent a magnesium isotopic anomaly. In either case, the initial magnesium isotopic composition of *Axtell 2271* was likely nonsolar. We also note that a large positive $\delta^{26}Mg_0$ value of $45 \pm 16‰$ was reported from *HAL*-like inclusion *DH-H1* (Ireland et al., 1992).

4.4. Variations in $(^{26}Al/^{27}Al)_0$ among FUN CAIs

Five out of the six FUN CAIs show inferred initial $^{26}Al/^{27}Al$ ratios resolvable from zero: $(3.1 \pm 1.6) \times 10^{-6}$ (*Axtell 2271*), $(3.7 \pm 1.5) \times 10^{-6}$ (*BG82DH8*), $(2.2 \pm 1.1) \times 10^{-6}$ (*C1*), $(1.5 \pm 1.1) \times 10^{-5}$ (*CG-14*), and $(5.3 \pm 0.9) \times 10^{-5}$ (*TE*); an upper limit of 4.7×10^{-5} for $(^{26}Al/^{27}Al)_0$ was determined in *EK1-4-1*. In Fig. 9, these results are plotted together with $(^{26}Al/^{27}Al)_0$ values in all FUN CAIs and *HAL*-like hibonite inclusions studied to date. There is a range of $(^{26}Al/^{27}Al)_0$ from $(5.2 \pm 1.7) \times 10^{-8}$ in *HAL* (Fahey et al., 1987) to nearly the canonical value in *Egg-3* (Wasserburg et al., 2012) and *TE* (El Goresy et al., 1991; this study). The variable and generally low $(^{26}Al/^{27}Al)_0$ values in FUN CAIs compared to the rather uniform $(^{26}Al/^{27}Al)_0$ of $\sim 5 \times 10^{-5}$ in normal CV CAIs (Kita et al., 2013) may reflect either late formation of FUN CAIs after decay of a significant amount of ^{26}Al or heterogeneity in the ^{26}Al distribution in the CAI-forming region(s) as discussed below.

4.4.1. Late-stage formation of FUN CAIs

The late-stage formation scenario of FUN CAIs is based on the assumption of a uniform distribution of ^{26}Al in the solar nebula at approximately the canonical value (Lee et al., 1979; Wasserburg et al., 2012). There are several problems with this scenario:

1. The late-stage formation of FUN CAIs after nearly complete decay of ^{26}Al is in conflict with the general consensus that ^{26}Al was a major heat source on the chondrite parent asteroids (e.g., Huss et al., 2006). The Allende meteorite contains FUN CAIs with a large range of $(^{26}Al/^{27}Al)_0$ (Fig. 10) and is one of the most metamorphosed CV3 chondrites (Bonal et al., 2006). The estimated peak metamorphic temperature reached by Allende is ~800 K (Weinbruch et al., 1994). If the Allende parent asteroid accreted after incorporation of the FUN CAI having the lowest $(^{26}Al/^{27}Al)_0$ of $(5.2 \pm 1.7) \times 10^{-8}$, *HAL* (Fahey et al., 1987), ^{26}Al decay could not have provided sufficient heat to generate this peak metamorphic temperature.
2. Decoupling between the ^{182}Hf-^{182}W and ^{26}Al-^{26}Mg chronologies was recently reported for the Allende FUN CAI *STP-1* (Holst et al., 2013). The inferred initial $^{182}Hf/^{180}Hf$ ratio of $(9.60 \pm 1.10) \times 10^{-5}$ of *STP-1* (Holst et al., 2013) is identical within analytical uncertainty to the $(^{182}Hf/^{180}Hf)_0$ of $(9.85 \pm 0.40) \times 10^{-5}$ in CV CAIs with the canonical $(^{26}Al/^{27}Al)_0$ (Burkhardt et al., 2012b). In contrast, the inferred $(^{26}Al/^{27}Al)_0$ in *STP-1* is $(2.94 \pm 0.21) \times 10^{-6}$, significantly lower than the canonical value. Because short-lived radionuclide ^{182}Hf ($t_{1/2}$ ~9 Ma) appears to have been uniformly distributed in the early Solar System (Kleine et al., 2005; Burkhardt et al., 2012b), the decoupling between ^{182}Hf and ^{26}Al in *STP-1* strongly suggests that ^{26}Al was heterogeneously distributed in the FUN CAI-forming region.
3. Late-stage formation of FUN CAIs requires the preservation of magnesium isotopic heterogeneity as well as other isotopic anomalies (e.g., calcium and titanium) in the CAI-forming region(s) for several million years. Although stable-isotope anomalies are observed in bulk chondrites and achondrites (e.g., Trinquier et al., 2009; Burkhardt et al., 2012a), the magnitudes of these anomalies are much smaller than those found in FUN inclusions.

4.4.2. *^{26}Al heterogeneity and early formation of FUN CAIs*

If FUN CAIs did not form "late", the low and variable $(^{26}Al/^{27}Al)_0$ in FUN CAIs most likely reflect heterogeneity of ^{26}Al in the early Solar System (Fahey et al., 1987; Sahijpal and Goswami, 1998; Thrane et al., 2008; Liu et al., 2009; Holst et al., 2013). Because the protoplanetary disk is expected to become well-mixed within several hundred to several thousand years (Boss, 2008, 2011), ^{26}Al heterogeneity in the earliest stage of the protoplanetary disk evolution is invoked to explain the variable $(^{26}Al/^{27}Al)_0$ in FUN CAIs (e.g., Mishra and Chaussidon, 2014).

Sahijpal and Goswami (1998) proposed late injection of ^{26}Al into the protosolar molecular cloud followed by homogenization during subsequent collapse of the cloud core to explain the ^{26}Al heterogeneity in CM hibonites and FUN CAIs. This model appears to be consistent with the apparent mutual exclusivity relationship of ^{26}Al with titanium isotopic anomalies (δ^{50}Ti) observed in CM hibonites (Clayton et al., 1988; Ireland et al., 1988; Sahijpal et al., 2000; Liu et al., 2009; Kööp et al., 2016). To explain these observations, Sahijpal et al. (2000) proposed the following scenario for the origin of refractory inclusions: (1) hibonite with Group III or ultrarefractory rare earth element (REE) patterns condensed prior to the injection of ^{26}Al into the protosolar molecular cloud; (2) *HAL*-like hibonite grains and FUN CAIs with low and variable $(^{26}Al/^{27}Al)_0$ and "small" isotopic anomalies formed during mixing and homogenization of the injected ^{26}Al; and (3) refractory grains and inclusions with canonical $(^{26}Al/^{27}Al)_0$ and Group II REE patterns condensed later, after nearly complete homogenization of ^{26}Al and isotopic anomalies in the protoplanetary disk. Although this scenario is supported by numerical modeling of protoplanetary disk evolution (Yang and Ciesla, 2012), it fails to provide an explanation for the apparent bimodal distribution of $(^{26}Al/^{27}Al)_0$ in corundum, hibonite, and grossite-rich CAIs from unmetamorphosed chondrites (Krot et al., 2012 and references therein).

In contrast, Trinquier et al. (2009) and Paton et al. (2013) attributed ^{26}Al heterogeneity to thermal processing (incomplete sublimation) of primordial solids in the protoplanetary disk. This processing resulted in preferential destruction of hypothetical thermally unstable ^{26}Al carriers initially uniformly distributed in the protoplanetary disk. Stable-isotope anomalies, including the magnesium isotopic heterogeneity observed in FUN CAIs and refractory grains, could have resulted from the thermal processing of primordial dust in the disk as well. The magnitude of isotopic anomalies is not necessarily related to the initial ^{26}Al abundances in these refractory objects (Holst et al., 2013). This scenario may have some difficulties explaining the Group II REE patterns, observed in some FUN inclusions, including *EK1-4-1* (Nagasawa et al., 1982), *CH-A5* (Sahijpal et al., 2000), *Mur-B1* (Liu et al., 2009), and *STP-1* (Holst et al., 2013), because Group II REE patterns are believed to reflect condensation from a gas depleted in the most refractory REEs. To overcome this problem, Holst et al. (2013) suggested that FUN CAI precursors are a mixture of condensates from a gas of solar composition and isotopically anomalous solids. This idea was also proposed by Ireland and Fegley (2000) to explain isotopic anomalies and low ^{26}Al in PLACs.

4.5. Scenario for FUN CAI formation

Similar to Ireland and Fegley (2000) and Holst et al. (2013), we infer that FUN CAI precursors are a mixture of condensates from a gas of solar composition and isotopically anomalous solids. We propose the following three-stage scenario for the formation of FUN CAIs.

1. Condensation of isotopically normal solids from a gaseous reservoir of approximately solar composition, indicated by the ^{16}O-rich compositions of most FUN CAIs (Krot et al., 2014) and Group II REE patterns in some of them (Nagasawa et al., 1982; Sahijpal et al., 2000; Liu et al., 2009; Holst et al., 2013).

2. Subsequent aggregation of these solids together with isotopically anomalous materials. The latter may have formed by selective destruction of isotopically anomalous carriers during thermal processing in the protoplanetary disk (Ireland and Fegley, 2000; Huss et al., 2003; Huss, 2004; Trinquier et al., 2009; Burkhardt et al., 2012a).
3. Melting and partial evaporation of the isotopically diverse FUN CAI precursors accompanied by crystallization at various total pressures and temperatures and by evaporation to varying degrees, resulting in mass-dependent fractionation effects in magnesium, silicon, and oxygen, as demonstrated by melt-evaporation experiments of CAI-like precursors (Richter et al., 2002; Mendybaev et al., 2013, 2017). Subsequently, some FUN CAIs may have experienced partial melting and oxygen isotopic exchange with an ^{16}O-poor gas (Krot et al., 2014).

The proposed stages of FUN CAI formation occurred during injection of ^{26}Al into the protosolar molecular cloud and homogenization in the protoplanetary disk, largely prior to the formation of CAIs with the canonical $(^{26}Al/^{27}Al)_0$ (Sahijpal and Goswami, 1998). This scenario may explain the generally low but variable $(^{26}Al/^{27}Al)_0$ of FUN CAIs.

Finally, we infer that FUN and non-FUN igneous CAIs formed by the same processes, including evaporation/condensation, aggregation, melting and evaporation in the CAI-forming region(s). The proposed scenario is generic, and could be applied to refractory inclusions of all types (FUN, F, UN, and normal). The fact that $\delta^{26}Mg_0$ and $(^{26}Al/^{27}Al)_0$ values of FUN CAIs are variable and extend to the levels found in normal, non-FUN CAIs, is consistent with this scenario.

5. CONCLUSIONS

We reported *in situ* high-precision magnesium isotopic measurements of individual minerals in six previously identified FUN CAIs, including *Axtell 2271* from Axtell, and *BG82DH8*, *C1*, *EK-1-4-1*, *CG-14*, and *TE* from Allende using the UH Cameca ims-1280 SIMS.

We find that the degree of mass-dependent fractionation of magnesium isotopes in an individual FUN CAI is generally consistent with the inferred mineral crystallization sequence, supporting an origin by igneous crystallization accompanied by evaporation. The wide range of magnesium mass fractionation (~3–18‰/amu) among hibonite grains in *Axtell 2271* may have resulted from back-reaction.

Most FUN CAIs studied show evidence for ^{26}Mg excess produced by the decay of ^{26}Al. The variable and large deficits of $\delta^{26}Mg_0$ in FUN CAIs provide evidence for magnesium isotopic heterogeneity in the early Solar System. The inferred initial $^{26}Al/^{27}Al$ ratios in FUN CAIs are generally low and variable up to the canonical value of $\sim 5.2 \times 10^{-5}$. We conclude that FUN CAIs formed earlier than or contemporaneously with the canonical CAIs and recorded heterogeneous distribution of ^{26}Al in the early Solar System.

We propose the following scenario for the origin of FUN CAIs: (*i*) condensation of CAI precursors from an ^{16}O-rich gaseous reservoir of approximately solar composition, (*ii*) formation of CAI precursors by aggregation of these solids with variable abundances of isotopically anomalous grains, possible carriers of unidentified nuclear (UN) effects, and (*iii*) melting and partial evaporation of the isotopically diverse aggregates at various total pressures and temperatures. We infer that the proposed scenario for FUN CAIs can be also applied to non-FUN CAIs, and thus that they have continuous initial ^{26}Al abundances, mass-dependent fractionation effects, and isotopic anomalies.

ACKNOWLEDGEMENTS

This paper is dedicated to the memory of Ian D. Hutcheon who initiated and played a major role in this study. Samples of the FUN CAIs *Axtell 2271*, *C1*, *EK1-4-1*, and *BG82DH8* were kindly provided by Dr. G. J. Wasserburg from the Lunatic Asylum collection, which has been donated by him to the Smithsonian Museum. These samples will be available from the Smithsonian Museum upon request from the Curator (Dr. G. J. MacPherson). Samples of *CG-14* and *TE* were provided by Dr. S. B. Simon and Dr. A. M. Davis (University of Chicago). We thank G. J. Wasserburg for useful discussions until the last time of his life and pay tribute to his contribution and outstanding works in cosmochemistry. We also thank Dr. Curtis D. Williams and Dr. Christine Floss for their constructive reviews that helped improve the manuscript and Dr. Dimitri A. Papanastassiou for thoughtful comments and editorial handling. This work was supported by NASA grants NNX10AH76G and NNX12AJ01G (A. N. Krot, PI) and NNX09AG39G and NNX15AF78G (A. M. Davis, PI), and Korea Polar Research Institute project PM16030 (C. Park). This is Hawai'i Institute of Geophysics and Planetology publication XXXX and School of Ocean and Earth Science and Technology publication XXXX.

APPENDIX A. SUPPLEMENTARY DATA

Supplementary data associated with this article can be found, in the online version, at http://dx.doi.org/10.1016/j.gca.2016.10.002.

REFERENCES

Beckett J. R. and Stolper E. (1994) The stability of hibonite, melilite and other aluminous phases in silicate melts: implications for the origin of hibonite-bearing inclusions from carbonaceous chondrites. *Meteoritics* **29**, 41–65.

Bizzarro M., Paton C., Larsen K., Schiller M., Trinquier A. and Ulfbeck D. (2011) High-precision Mg-isotope measurements of terrestrial and extraterrestrial material by HR-MC-ICPMS-implications for the relative and absolute Mg-isotope composition of the bulk silicate Earth. *J. Anal. Atom. Spectrom.* **26**, 565–577.

Bonal L., Quirico E., Bourot-Denise M. and Montagnac G. (2006) Determination of the petrologic type of CV3 chondrites by Raman spectroscopy of included organic matter. *Geochim. Cosmochim. Acta* **70**, 1849–1863.

Boss A. P. (2008) Mixing in the solar nebula: implications for isotopic heterogeneity and large-scale transport of refractory grains. *Earth Planet. Sci. Lett.* **268**, 102–109.

Boss A. P. (2011) Evolution of the solar nebula. IX. Gradients in the spatial heterogeneity of the short-lived radioisotopes ^{60}Fe and ^{26}Al and the stable oxygen isotopes. *Astrophys. J.* **739**, #61 (11 pp).

Brigham C. A. (1990) *Isotopic heterogeneity in calcium-aluminum-rich meteoritic inclusions* (Ph.D. thesis). California Institute of Technology, California, United States.

Bullock E. S., Tenner T. J., Nakashima D., Kita N. T., MacPherson G. J., Ivanova M. A., Krot A. N., Petaev M. I. and Jacobsen S. B. (2017) High precision Al-Mg systematics of forsterite-bearing Type B CAIs from CV3 chondrites. *Geochim. Cosmochim. Acta* **201**, 65–82.

Burkhardt C., Kleine T., Dauphas N. and Wieler R. (2012a) Origin of isotopic heterogeneity in the solar nebula by thermal processing and mixing of nebular dust. *Earth Planet. Sci. Lett.* **357**, 298–307.

Burkhardt C., Kleine T., Dauphas N. and Wieler R. (2012b) Nucleosynthetic tungsten isotope anomalies in acid leachates of the Murchison chondrite: implications for hafnium-tungsten chronometry. *Astrophys. J. Lett.* **753**, #L6 (7 pp).

Clayton R. N. and Mayeda T. K. (1977) Correlated oxygen and magnesium isotope anomalies in Allende inclusions, I: Oxygen. *Geophys. Res. Lett.* **4**, 295–298.

Clayton R. N., MacPherson G. J., Hutcheon I. D., Davis A. M., Grossman L., Mayeda T. K., Molini-Velsko C., Allen J. M. and Goresy A. E. (1984) Two forsterite-bearing FUN inclusions in the Allende meteorite. *Geochim. Cosmochim. Acta* **48**, 535–548.

Clayton R. N., Hinton R. W. and Davis A. M. (1988) Isotopic variations in the rock-forming elements in meteorites. *Philso. Trans. R. Soc. Lond.* **A325**, 483–501.

Connelly J. N., Bizzarro M., Krot A. N., Nordlund Å., Wielandt D. and Ivanova M. A. (2012) The absolute chronology and thermal processing of solids in the solar protoplanetary disk. *Science* **338**, 651–655.

Davis A. M., MacPherson G. J., Clayton R. N., Mayeda T. K., Sylvester P. J., Grossman L., Hinton R. W. and Laughlin J. R. (1991) Melt solidification and late-stage evaporation in the evolution of a FUN inclusion from the Vigarano C3V chondrite. *Geochim. Cosmochim. Acta* **55**, 621–637.

Davis A. M., Richter F. M., Mendybaev R. A., Janney P. E., Wadhwa M., McKeegan K. D. and Stansbery E. (2005) Isotopic mass fractionation laws and the initial Solar System ^{26}Al/^{27}Al ratio. *Lunar Planet. Sci.* **36**, #2334.

Davis A. M., Richter F. M., Mendybaev R. A., Janney P. E., Wadhwa M. and McKeegan K. D. (2015) Isotopic mass fractionation laws for magnesium and their effects on ^{26}Al-^{26}Mg systematics in solar system materials. *Geochim. Cosmochim. Acta* **158**, 245–261.

Dominik B., Jessberger E. K., Staudacher T. H., Nagel K. and El Goresy A. (1978) A new type of white inclusion in Allende: Petrography, mineral chemistry, ^{40}Ar-^{39}Ar ages, and genetic implications. *Proc. Lunar Planet. Sci.* **9**, 1249–1266.

El Goresy A., Zinner E., Caillet C., Virag A. and Weinbruch S. (1991) Allende TE: evidence for multiple isotopic fractionation events before and after oxidation and alteration. *Lunar Planet. Sci.* **22**, 345.

Esat T. M., Lee T., Papanastassiou D. A. and Wasserburg G. J. (1978) Search for ^{26}Al effects in the Allende FUN inclusion C1. *Geophys. Res. Lett.* **5**, 807–810.

Fahey A. J., Goswami J. N., McKeegan K. D. and Zinner E. K. (1987) ^{26}Al, ^{244}Pu, ^{50}Ti, REE, and trace element abundances in hibonite grains from CM and CV meteorites. *Geochim. Cosmochim. Acta* **51**, 329–350.

Fintor K., Park C., Nagy S., Pál-Molnár E. and Krot A. N. (2014) Hydrothermal origin of hexagonal $CaAl_2Si_2O_8$ (dmisteinbergite) in a compact type A CAI from the Northwest Africa 2086 CV3 chondrite. *Meteorit. Planet. Sci.* **49**, 812–823.

Fukuda K., Hiyagon H., Sasaki S., Fujiya W., Takahata N., Sano Y. and Morishita Y. (2013) An ion microprobe study of FUN-like hibonite-bearing inclusions from the Murchison (CM2) meteorite. *Lunar Planet. Sci.* **44**, 1870.

Hiyagon H. and Hashimoto A. (2008) Isotopic and rare earth element studies of a FUN-like forsterite-bearing Inclusion from Allende. *Meteorit. Planet. Sci. (Suppl.)* **43**, #5128.

Holst J. C., Olsen M. B., Paton C., Nagashima K., Schiller M., Wielandt D., Larsen K. K., Connelly J. N., Jørgensen J. K., Krot A. N., Nordlund Å. and Bizzarro M. (2013) ^{182}Hf-^{182}W age dating of a ^{26}Al-poor inclusion and implications for the origin of short-lived radioisotopes in the early Solar System. *Proc. Natl. Acad. Sci.* **110**, 8819–8823.

Huss G. R., Meshik A. P., Smith J. B. and Hohenberg C. M. (2003) Presolar diamond, silicon carbide, and graphite in carbonaceous chondrites: Implications for thermal processing in the solar nebula. *Geochim. Cosmochim. Acta* **67**, 4823–4848.

Huss G. R., Rubin A. E. and Grossman J. N. (2006) Thermal metamorphism in chondrites. In *Meteorites and the Early Solar System II* (eds. D. S. Lauretta and , Jr.H. Y. McSween). The University of Arizona Press, Tucson, pp. 567–586.

Huss G. R. (2004) Implications of isotopic anomalies and presolar grains for the formation of the solar system. *Antarc. Meteorit. Res.* **17**, 132–152.

Hutcheon I. D. (1982) Ion probe magnesium isotopic measurements of Allende inclusions. *Amer. Chem. Soc. Symp. Ser.* **176**, 95–128.

Ireland T. R. and Compston W. (1987) Large heterogeneous ^{26}Mg excesses in a hibonite from the Murchison meteorite. *Nature* **327**, 689–692.

Ireland T. R. and Fegley B. (2000) The solar system's earliest chemistry: systematics of refractory inclusions. *Int. Geol. Rev.* **42**, 865–894.

Ireland T. R., Compston W. and Esat T. M. (1986) Magnesium isotopic compositions of olivine, spinel, and hibonite from the Murchison carbonaceous chondrite. *Geochim. Cosmochim. Acta* **50**, 1413–1421.

Ireland T. R., Fahey A. J. and Zinner E. K. (1988) Trace-element abundances in hibonites from the Murchison carbonaceous chondrite: Constraints on high-temperature processes in the solar nebula. *Geochim. Cosmochim. Acta* **52**, 2841–2854.

Ireland T. R., Fahey A. J. and Zinner E. K. (1991) Hibonite-bearing microspherules: A new type of refractory inclusions with large isotopic anomalies. *Geochim. Cosmochim. Acta* **55**, 367–379.

Ireland T. R., Zinner E. K., Fahey A. J. and Esat T. M. (1992) Evidence for distillation in the formation of HAL and related hibonite inclusions. *Geochim. Cosmochim. Acta* **56**, 2503–2520.

Ito M. and Ganguly J. (2009) Mg diffusion in minerals in CAIs: New experimental data for melilites and implications for the Al-Mg chronometer and thermal history of CAIs. *Lunar Planet. Sci.* **40**, #1753.

Jacobsen B., Yin Q., Moynier F., Amelin Y., Krot A. N., Nagashima K., Hutcheon I. D. and Palme H. (2008a) ^{26}Al-^{26}Mg and ^{207}Pb-^{206}Pb systematics of Allende CAIs: Canonical solar initial ^{26}Al/^{27}Al ratio reinstated. *Earth Planet. Sci. Lett.* **272**, 353–364.

Jacobsen S. B., Chakrabarti R., Ranen M. C. and Petaev M. I. (2008b) High resolution ^{26}Al-^{26}Mg chronometry of CAIs from the Allende meteorite. *Lunar Planet. Sci.* **39**, #1999.

Jungck M. H. A., Shimamura T. and Lugmair G. W. (1984) Ca isotope variations in Allende. *Geochim. Cosmochim. Acta* **48**, 2651–2658.

Kita N. T., Ushikubo T., Knight K. B., Mendybaev R. A., Davis A. M., Richter F. M. and Fournelle J. H. (2012) Internal ^{26}Al-^{26}Mg isotope systematics of a Type B CAI: Remelting of refractory precursor solids. *Geochim. Cosmochim. Acta* **86**, 37–51.

Kita N. T., Yin Q.-Z., MacPherson G. J., Ushikubo T., Jacobsen B., Nagashima K., Kurahashi E., Krot A. N. and Jacobsen S. B. (2013) ^{26}Al-^{26}Mg isotope systematics of the first solids in the early solar system. *Meteorit. Planet. Sci.* **48**, 1383–1400.

Kleine T., Mezger K., Palme H., Scherer E. and Münker C. (2005) Early core formation in asteroids and late accretion of chondrite parent bodies: Evidence from ^{182}Hf-^{182}W in CAIs, metal-rich chondrites, and iron meteorites. *Geochim. Cosmochim. Acta* **69**, 5805–5818.

Kööp L., Davis A. M., Nakashima D., Park C., Krot A. N., Nagashima K., Tenner T. J., Heck P. R. and Kita N. T. (2016) A link between oxygen, calcium and titanium isotopes in ^{26}Al-poor hibonite-rich CAIs from Murchison and implications for the heterogeneity of dust reservoirs in the solar nebula. *Geochim. Cosmochim. Acta* **189**, 70–95.

Krot A. N., Nagashima K., Ciesla F. J., Meyer B. S., Hutcheon I. D., Davis A. M., Huss G. R. and Scott E. R. D. (2010) Oxygen isotopic composition of the Sun and mean oxygen isotopic composition of the protosolar silicate dust: Evidence from refractory inclusions. *Astrophys. J.* **713**, 1159–1166.

Krot A. N., Makide K., Nagashima K., Huss G. R., Ogliore R. C., Ciesla F. J., Yang L., Hellebrand E. and Gaidos E. (2012) Heterogeneous distribution of ^{26}Al at the birth of the solar system: Evidence from refractory grains and inclusions. *Meteorit. Planet. Sci.* **47**, 1948–1979.

Krot A. N., Nagashima K., Wasserburg G. J., Huss G. R., Papanastassiou D. A., Davis A. M., Hutcheon I. D. and Bizzarro M. (2014) Calcium-aluminum-rich inclusions with fractionation and unknown nuclear effects (FUN CAIs): I. Mineralogy, petrology, and oxygen isotopic compositions. *Geochim. Cosmochim. Acta* **145**, 206–247.

Larsen K. K., Trinquier A., Paton C., Schiller M., Wielandt D., Ivanova M. A., Connelly J. N., Nordlund Å., Krot A. N. and Bizzarro M. (2011) Evidence for magnesium isotope heterogeneity in the solar protoplanetary disk. *Astrophys. J. Lett.* **735**, #L37 (7 pp).

Lee T., Papanastassiou D. A. and Wasserburg G. J. (1976) Demonstration of ^{26}Mg excess in Allende and evidence for ^{26}Al. *Geophys. Res. Lett.* **3**, 41–44.

Lee T., Papanastassiou D. A. and Wasserburg G. J. (1977) Aluminum-26 in the early solar system-Fossil or fuel. *Astrophys. J. Lett.* **211**, L107–L110.

Lee T., Russell W. A. and Wasserburg G. J. (1979) Calcium isotopic anomalies and the lack of aluminum-26 in an unusual Allende inclusion. *Astrophys. J. Lett.* **228**, L93–L98.

Lee T., Mayeda T. K. and Clayton R. N. (1980) Oxygen isotopic anomalies in Allende inclusion HAL. *Geophys. Res. Lett.* **7**, 493–496.

Liu M.-C. and McKeegan K. D. (2009) On an irradiation origin for magnesium isotope anomalies in meteoritic hibonite. *Astrophys. J. Lett.* **697**, L145–L148.

Liu M.-C., McKeegan K. D., Goswami J. N., Marhas K. K., Sahijpal S., Ireland T. R. and Davis A. M. (2009) Isotopic records in CM hibonites: Implications for timescales of mixing of isotope reservoirs in the solar nebula. *Geochim. Cosmochim. Acta* **73**, 5051–5079.

Liu M.-C., Chaussidon M., Göpel C. and Lee T. (2012) A heterogeneous solar nebula as sampled by CM hibonite grains. *Earth Planet. Sci. Lett.* **327**, 75–83.

Loss R. D., Lugmair G. W., Davis A. M. and MacPherson G. J. (1994) Isotopically distinct reservoirs in the solar nebula: Isotope anomalies in Vigarano meteorite inclusions. *Astrophys. J. Lett.* **436**, L193–L196.

Ludwig K. (2003) ISOPLOT: A Geochronological Toolkit for Microsoft Excel 3.00. Berkeley Geochronology Center Special Publication No. 4, Berkeley, CA 94709.

MacPherson G. J., Davis A. M. and Zinner E. K. (1995) The distribution of aluminum-26 in the early Solar System—A reappraisal. *Meteoritics* **30**, 365–386.

MacPherson G. J., Kita N. T., Ushikubo T., Bullock E. S. and Davis A. M. (2012) Well-resolved variations in the formation ages for Ca-Al-rich inclusions in the early Solar System. *Earth Planet. Sci. Lett.* **331**, 43–54.

Makide K., Nagashima K., Krot A. N., Huss G. R., Hutcheon I. D. and Bischoff A. (2009) Oxygen- and magnesium-isotope compositions of calcium-aluminum-rich inclusions from CR2 carbonaceous chondrites. *Geochim. Cosmochim. Acta* **73**, 5018–5050.

Marin-Carbonne J., McKeegan K. D., Davis A. M., MacPherson G. J., Mendybaev R. A. and Richter F. M. (2012) O, Si and Mg isotopic compositions of FUN inclusion Vigarano 1623–5. *Lunar Planet. Sci.* **43**, #1687.

McCulloch M. T. and Wasserburg G. J. (1978a) More anomalies from the Allende meteorite: Samarium. *Geophys. Res. Lett.* **5**, 599–602.

McCulloch M. T. and Wasserburg G. J. (1978b) Barium and neodymium isotopic anomalies in the Allende meteorite. *Astrophys. J. Lett.* **220**, L15–L19.

McKeegan K. D., Davis A. M., Taylor D. J. and MacPherson G. J. (2005) In-situ investigation of Mg isotope compositions in a FUN inclusion. *Lunar Planet. Sci.* **36**, #2077.

Mendybaev R. A., Richter F. M., Georg R. B., Janney P. E., Spicuzza M. J., Davis A. M. and Valley J. W. (2013) Experimental evaporation of Mg- and Si-rich melts: Implications for the origin and evolution of FUN CAIs. *Geochim. Cosmochim. Acta* **123**, 368–384.

Mendybaev R. A., Williams C. D., Spicuzza M. J., Richter F. M., Valley J. W., Fedkin A. V. and Wadhwa M. (2017) Thermal and chemical evolution in the early Solar System as recorded by FUN CAIs: Part II - Laboratory evaporation of potential CMS-1 precursor material. *Geochim. Cosmochim. Acta* **201**, 49–64.

Mishra R. K. and Chaussidon M. (2014) Timing and extent of Mg and Al isotopic homogenization in the early inner Solar System. *Earth Planet. Sci. Lett.* **390**, 318–326.

Nagahara H. and Ozawa K. (2012) The role of exchange reactions in oxygen isotope fractionation during CAI and chondrule formation. *Meteorit. Planet. Sci.* **47**, 1209–1228.

Nagasawa H., Blanchard D. P., Shimizu H. and Masuda A. (1982) Trace element concentrations in the isotopically unique Allende inclusion, EK 1-4-1. *Geochim. Cosmochim. Acta* **46**, 1669–1673.

Niederer F. R. and Papanastassiou D. A. (1984) Ca isotopes in refractory inclusions. *Geochim. Cosmochim. Acta* **48**, 1279–1293.

Niederer F. R., Papanastassiou D. A. and Wasserburg G. J. (1981) The isotopic composition of titanium in the Allende and Leoville meteorites. *Geochim. Cosmochim. Acta* **45**, 1017–1031.

Niederer F. R., Papanastassiou D. A. and Wasserburg G. J. (1985) Absolute isotopic abundances of Ti in meteorites. *Geochim. Cosmochim. Acta* **49**, 835–851.

Ogliore R. C., Huss G. R. and Nagashima K. (2011) Ratio estimation in SIMS analysis. *Nucl. Instrum. Methods Phys. Res. B* **269**, 1910–1918.

Palme H., Lodders K., and Jones A. (2014) Solar system abundances of the elements. In *Planets, Asteroids, Comets, and the Solar System* (ed. A. M. Davis). Vol. 2. Treatise on Geochemistry, 2nd ed. (eds. H. D. Holland, K. K. Turekian). Elsevier, Oxford, pp. 15–36.

Papanastassiou D. A. and Brigham C. A. (1987) FUN isotopic anomalies: Reincarnation in purple refractory inclusions. *Lunar Planet. Sci.* **18**, #756.

Papanastassiou D. A. and Brigham C. A. (1989) The identification of meteorite inclusions with isotope anomalies. *Astrophys. J. Lett.* **338**, L37–L40.

Papanastassiou D. A. and Wasserburg G. J. (1978) Strontium isotopic anomalies in the Allende meteorite. *Geophys. Res. Lett.* **5**, 595–598.

Papanastassiou D. A. (1986) Chromium isotopic anomalies in the Allende meteorite. *Astrophys. J. Lett.* **308**, L27–L30.

Park C., Nagashima K., Ma C., Krot A. N. and Bizzarro M. (2013) Two generations of hexagonal $CaAl_2Si_2O_8$ (dmisteinbergite) in the Type B2 FUN CAI STP-1. *Meteorit. Planet. Sci. (Suppl.)* **48**, #5048.

Paton C., Schiller M. and Bizzarro M. (2013) Identification of an ^{84}Sr-depleted carrier in primitive meteorites and implications for thermal processing in the solar protoplanetary disk. *Astrophys. J. Lett.* **763**, #L40 (6 pp).

Podosek F. A., Zinner E. K., Macpherson G. J., Lundberg L. L., Brannon J. C. and Fahey A. J. (1991) Correlated study of initial ^{87}Sr/^{86}Sr and Al-Mg isotopic systematics and petrologic properties in a suite of refractory inclusions from the Allende meteorite. *Geochim. Cosmochim. Acta* **55**, 1083–1110.

Richter F. M., Davis A. M., Ebel D. S. and Hashimoto A. (2002) Elemental and isotopic fractionation of Type B calcium-, aluminum-rich inclusions: experiments, theoretical considerations, and constraints on their thermal evolution. *Geochim. Cosmochim. Acta* **66**, 521–540.

Russell W. A., Papanastassiou D. A. and Tombrello T. A. (1978) Ca isotope fractionation on the Earth and other solar system materials. *Geochim. Cosmochim. Acta* **42**, 1075–1090.

Russell S. S., Huss G. R., Fahey A. J., Greenwood R. C., Hutchison R. and Wasserburg G. J. (1998) An isotopic and petrologic study of calcium-aluminum-rich inclusions from CO3 meteorites. *Geochim. Cosmochim. Acta* **62**, 689–714.

Sahijpal S. and Goswami J. N. (1998) Refractory phases in primitive meteorites devoid of ^{26}Al and ^{41}Ca: Representative samples of first Solar System solids? *Astrophys. J. Lett.* **509**, L137–L140.

Sahijpal S., Goswami J. N. and Davis A. M. (2000) K, Mg, Ti and Ca isotopic compositions and refractory trace element abundances in hibonites from CM and CV meteorites: Implications for early solar system processes. *Geochim. Cosmochim. Acta* **64**, 1989–2005.

Simon J. I. and Young E. D. (2011) Resetting, errorchrons and the meaning of canonical CAI initial ^{26}Al/^{27}Al values. *Earth Planet. Sci. Lett.* **304**, 468–482.

Srinivasan G., Huss G. R. and Wasserburg G. J. (2000) A petrographic, chemical, and isotopic study of calcium-aluminum-rich inclusions and aluminum-rich chondrules from the Axtell (CV3) chondrite. *Meteorit. Planet. Sci.* **35**, 1333–1354.

Stolper E. (1982) Crystallization sequences of Ca-Al-rich inclusions from Allende: An experimental study. *Geochim. Cosmochim. Acta* **46**, 2159–2180.

Sugiura N. and Krot A. N. (2007) ^{26}Al-^{26}Mg systematics of Ca-Al-rich inclusions, amoeboid olivine aggregates, and chondrules from the ungrouped carbonaceous chondrite Acfer 094. *Meteorit. Planet. Sci.* **42**, 1183–1195.

Thrane K., Nagashima K., Krot A. N. and Bizzarro M. (2008) Discovery of a new FUN CAI from a CV carbonaceous chondrite: Evidence for multistage thermal processing in the protoplanetary disk. *Astrophys. J. Lett.* **680**, L141–L144.

Trinquier A., Elliott T., Ulfbeck D., Coath C., Krot A. N. and Bizzarro M. (2009) Origin of nucleosynthetic isotope heterogeneity in the solar protoplanetary disk. *Science* **324**, 374–376.

Ushikubo T., Hiyagon H. and Sugiura N. (2007) A FUN-like hibonite inclusion with a large ^{26}Mg-excess. *Earth Planet. Sci. Lett.* **254**, 115–126.

Wasserburg G., Lee T. and Papanastassiou D. (1977) Correlated O and Mg isotopic anomalies in Allende inclusions: II. Magnesium. *Geophys. Res. Lett.* **4**, 299–302.

Wasserburg G. J., Wimpenny J. and Yin Q.-Z. (2012) Mg isotopic heterogeneity, Al-Mg isochrons, and canonical ^{26}Al/^{27}Al in the early solar system. *Meteorit. Planet. Sci.* **47**, 1980–1997.

Weinbruch S., Armstrong J. and Palme H. (1994) Constraints on the thermal history of the Allende parent body as derived from olivine-spinel thermometry and Fe/Mg interdiffusion in olivine. *Geochim. Cosmochim. Acta* **58**, 1019–1030.

Williams C. D., Wadhwa M., Janney P. E., Hines R. R., Bullock E. S. and MacPherson G. J. (2012) Ti, Si and Mg isotope systematics of FUN CAI CMS-1. *Meteorit. Planet. Sci. (Suppl.)* **47**, #5102.

Williams C. D., Ushikubo T., MacPherson G. J., Bullock E. S., Kita N. T. and Wadhwa M. (2013) Oxygen isotope systematics of Allende FUN CAI CMS-1. *Lunar Planet. Sci.* **44**, #1719.

Yang L. and Ciesla F. J. (2012) The effects of disk building on the distributions of refractory materials in the solar nebula. *Meteorit. Planet. Sci.* **47**, 99–119.

Young E. D., Galy A. and Nagahara H. (2002) Kinetic and equilibrium mass-dependent isotope fractionation laws in nature and their geochemical and cosmochemical significance. *Geochim. Cosmochim. Acta* **66**, 1095–1104.

Zinner E., Virag A., Weinbruch S. and El Goresy A. (1989) Allende TE revisited II: Magnesium and oxygen isotopic stratigraphy. *Meteoritics* **24**, #345.

Associate editor: Dimitri A. Papanastassiou